Stabilization of Interdomain Interactions in G protein α_i Subunits Determines $G\alpha_i$ Subtype Signaling Specificity

Tyler J. Lefevre[1,2], Wenyuan Wei[4†], Elizaveta Mukhaleva[4†], Sai Pranathi Meda Venkata[1], Naincy R. Chandan[1,3], Saji Abraham[1], Yong Li[4], Carmen W. Dessauer[4], Nagarajan Vaidehi[5], and Alan V. Smrcka[1*]

[1]Department of Pharmacology, University of Michigan Medical School, Ann Arbor, MI; [2]Program in Chemical Biology, University of Michigan, Ann Arbor, MI; [3]Genentech, South San Francisco, CA; [4]Department of Integrative Biology and Pharmacology McGovern Medical School, UTHealth, Houston, TX; [5]Department of Computational and Quantitative Medicine, Beckman Research Institute of the City of Hope, Duarte, CA

*Correspondence:

Alan V. Smrcka, Ph.D.

Email: avsmrcka@umich.edu

Phone: 734-615-4945

[†]These authors contributed equally.

Abstract

Highly homologous members of the $G\alpha_i$ family, $G\alpha_{i1\text{-}3}$, have distinct tissue distributions and physiological functions, yet the functional properties of these proteins with respect to GDP/GTP binding and regulation of adenylate cyclase are very similar. We recently identified PDZ-RhoGEF (PRG) as a novel $G\alpha_{i1}$ effector, however, it is poorly activated by $G\alpha_{i2}$. Here, in a proteomic proximity labeling screen we observed a strong preference for $G\alpha_{i1}$ relative to $G\alpha_{i2}$ with respect to engagement of a broad range of potential targets. We investigated the mechanistic basis for this selectivity using PRG as a representative target. Substitution of either the helical domain (HD) from $G\alpha_{i1}$ into $G\alpha_{i2}$ or substitution of a single amino acid, A230 in $G\alpha_{i2}$ to the corresponding D in $G\alpha_{i1}$, largely rescues PRG activation and interactions with other $G\alpha_i$ targets. Molecular dynamics simulations combined with Bayesian network models revealed that in the GTP bound state, dynamic separation at the HD-Ras-like domain (RLD) interface is prevalent in $G\alpha_{i2}$ relative to $G\alpha_{i1}$ and that mutation of $A230^{s4h3.3}$ to D in $G\alpha_{i2}$ stabilizes HD-RLD interactions through formation of an ionic interaction with $R145^{HD.11}$ in the HD. These interactions in turn modify the conformation of Switch III. These data support a model where $D229^{s4h3.3}$ in $G\alpha_{i1}$ interacts with $R144^{HD.11}$ stabilizes a network of interactions between HD and RLD to promote protein target recognition. The corresponding A230 in $G\alpha_{i2}$ is unable to form the “ionic lock” to stabilize this network leading to an overall lower efficacy with respect to target interactions. This study reveals distinct mechanistic properties that could underly differential biological and physiological consequences of activation of $G\alpha_{i1}$ or $G\alpha_{i2}$ by GPCRs.

50 **Introduction**

51 Many physiologically important hormones and neurotransmitters signal through G
52 protein-coupled receptors (GPCRs), rendering these membrane-spanning receptors
53 highly clinically significant as important drug targets [1,2]. GPCRs transduce signals into
54 the cell via heterotrimeric G proteins, consisting of the Gα subunit and the Gβγ
55 constitutive heterodimer. Signaling diversity from GPCRs is primarily achieved via an
56 array of Gα subunit protein families which harbor distinct downstream signaling
57 capabilities, including the G_s, $G_{i/o}$, $G_{q/11}$, and $G_{12/13}$ families [3-6].

58 Gα subunits consist of a Ras-like domain (RLD), which binds and hydrolyzes
59 guanine nucleotides, and an all-helical domain (HD), connected by a flexible hinge
60 region [5,7]. Much of the investigative focus on Gα protein function has been on the RLD,
61 which harbors three "Switch" regions (Switch I-III) that undergo conformational
62 alterations upon GTP binding. Upon binding GTP, Switch regions I-III collapse toward
63 the bound nucleotide in a conformational rearrangement that permits Gα·GTP-effector
64 interaction after separation from Gβγ and the receptor [8]. In contrast, the HD is relatively
65 rigid and opens along the interdomain cleft via the flexible hinge in the nucleotide free
66 transition state along the pathway of receptor-mediated GDP release [9-11]. Mutation of
67 residues along the Ras-HD interface further increases receptor-independent rate of
68 GDP dissociation in $G\alpha_i$ [12].

69 Generally, the $G\alpha_s$ family activates adenylyl cyclases (ACs) to produce 3',5'-
70 cyclic adenosine monophosphate (cAMP) and the $G\alpha_i$ family inhibits ACs [3]. The $G\alpha_{i/o}$
71 family consists of $G\alpha_{i1}$, $G\alpha_{i2}$, $G\alpha_{i3}$, $G\alpha_o$, $G\alpha_{T1}$, $G\alpha_{T2}$, $G\alpha_{T3}$, and $G\alpha_z$. $G\alpha_o$ is prominent in
72 the brain, $G\alpha_T$ in the visual and taste systems, and $G\alpha_z$ in the brain and prostate. $G\alpha_{i2}$

73 protein expression is more widespread and more abundant than any other protein in the
74 $G\alpha_{i/o}$ family, except for $G\alpha_o$ [13]. $G\alpha_{i1-3}$ are expressed broadly in humans, with $G\alpha_{i2}$ often
75 being expressed alongside $G\alpha_{i3}$ and/or $G\alpha_{i1}$. $G\alpha_{i1-3}$ subunits are 94% identical between
76 $G\alpha_{i1}$ and $G\alpha_{i3}$, 86% identical between $G\alpha_{i1}$ and $G\alpha_{i2}$, and 88% identical between $G\alpha_{i2}$
77 and $G\alpha_{i3}$ [14]. These three members of the $G\alpha_i$ subfamily have identical rates of single
78 turnover GTP hydrolysis, but the GDP dissociation rate from $G\alpha_{i2}$ is approximately two-
79 fold faster than for the other two isoforms [15].

80 In terms of signaling specificity, all $G\alpha_i$ subtypes inhibit various AC isoforms with
81 similar potency and efficacy [16]. For decades, AC was the only known effector of $G\alpha_i$.
82 Subsequently, a small number of proteins have been characterized as binding partners
83 of $G\alpha_i$: G protein-activated inwardly-rectifying potassium channels (GIRK) [17-20] [21],
84 epidermal growth factor receptor (EGFR), and growth factor receptor binding 2–
85 associated binding protein 1 (Gab1) [22], although the biochemical and biological
86 significance of these interactions is less well understood. Importantly, genetic deletion
87 or inactivation of endogenous individual $G\alpha_i$ isoforms have yielded evidence for
88 differential function in primary tissues and organisms. For example, knockout of $G\alpha_{i2}$ in
89 mice results in exacerbated ischemic injury and cardiac infarction, while mice lacking
90 $G\alpha_{i3}$ saw an upregulation in $G\alpha_{i2}$ and reduced injury [21,23-26]. Additionally, $G\alpha_{i2}$ primarily
91 promotes arrest and $G\alpha_{i3}$ is required for transmigration and chemotaxis in mouse
92 neutrophils [27], while $G\alpha_{i3}$ activation downstream of CXCR3 has been shown to inhibit
93 $G\alpha_{i2}$ activation in murine activated T cells [28]. These data strongly suggest that these
94 isoforms serve non-redundant, unique functions, yet the biochemical basis for driving

95 selective functionality has yet to be determined despite nearly three decades of
96 research.

97 Recently, our laboratory identified PDZ-RhoGEF (PRG) as a novel, direct effector
98 of $G\alpha_i$ in an unbiased proximity interaction screen [29]. $G\alpha_{i1}$ binds and activates PRG in a
99 nucleotide-dependent and receptor-dependent manner in cells. $G\alpha_{i3}$ also activates
100 PRG, but $G\alpha_{i2}$ only weakly stimulates PRG. Here, we have interrogated the nature of
101 the specificity of $G\alpha_i$ subfamily members for PRG at the molecular level. In doing so, we
102 have uncovered an atomic-level mechanism where the differences between $G\alpha_{i1}$ and
103 $G\alpha_{i2}$ with respect to the ability to stabilize interactions between the HD and the Switch III
104 region of the RLD results in weaker PRG engagement by $G\alpha_{i2}$. Follow-up with unbiased
105 proximity labeling coupled to tandem MS proteomics supports the idea that this
106 mechanism extends beyond PRG interactions to multiple additional $G\alpha_i$ targets. Overall,
107 our studies support a model in which the strength and frequency of interactions between
108 $G\alpha_i$ Switch III and the HD control the ability to bind and activate PRG and other target
109 proteins, differentiating $G\alpha_i$ subfamily structure and function.

110

111

112

113

114

115

116

117

118 **Results**

119 **$G\alpha_{i1}$ more effectively activates and interacts with PRG than $G\alpha_{i2}$**

120 We have previously shown [29] that $G\alpha_{i1}$ stimulates PRG and subsequent RhoA
121 activation in a manner dependent on the activation state of $G\alpha_i$. To mimic that GTP
122 bound state of $G\alpha_i$, a catalytic glutamine 204 was substituted with leucine which strongly
123 inhibits GTP hydrolysis leading to constitutive GTP binding and activation [7,30-32].
124 Transient co-expression of $G\alpha_{i1}$ Q204L ($G\alpha_{i1}$ QL), PRG, and an SRE-luciferase plasmid
125 that reports on RhoA activation in HEK293 cells (Fig. 1A) results in significant PRG
126 activation (Fig. 1B). $G\alpha_{i2}$ Q205L ($G\alpha_{i2}$ QL) only weakly activates PRG activity in the
127 same assay. Concentration-response experiments show a significant difference in the
128 efficacy of PRG activation by $G\alpha_{i1}$ QL and $G\alpha_{i2}$ QL (Fig. 1C). This indicates that the
129 difference is not due to differences in GTP binding since this would alter the potency of
130 activation rather than efficacy. There is some variability in this assay with respect to the
131 fold activation of PRG by $G\alpha_i$ but the differences between $G\alpha_{i1}$ and $G\alpha_{i2}$ remain
132 internally consistent within each assay set.

133 To validate PRG-$G\alpha_i$ interactions in cells, we performed a NanoBiT
134 nanoluciferase complementation assay [33], in which the NanoLuc LgBiT was inserted
135 after the αA helix in Gα subunits [34], and NanoLuc SmBiT was appended to the prior to
136 the N-terminal Myc tag of myc-PRG (Fig. 1D). Coexpressing $G\alpha_{i1}$ QL-LgBiT with SmBiT-
137 PRG in HEK293 cells resulted in an increase in luminescent signal relative to $G\alpha_{i1}$ WT-

138 LgBiT, indicating a nucleotide-dependent interaction with PRG. This was not observed
139 for QL variants in $G\alpha_{i2}$, $G\alpha_s$, or $G\alpha_q$ (Fig. 1E). Together, these results show that $G\alpha_{i1}$
140 interacts with, and activates PRG in a GTP-dependent manner, while $G\alpha_{i2}$ is much less
141 efficient in this interaction.

142 **Active $G\alpha_{i2}$ QL BioID weakly engages the proximal interactome relative to $G\alpha_{i1}$ QL**
143 **BioID**

144 Given their previously known functional overlap, the stark disparity between $G\alpha_{i1}$
145 and $G\alpha_{i2}$ in their ability to activate PRG prompted us to probe for further examples of
146 selectivity between $G\alpha_i$ subtypes. PRG was initially identified as a novel target of $G\alpha_{i1}$
147 using unbiased BioID2 proximity labeling coupled to mass spectrometry. BioID2
148 functionalizes biotin releasing reactive biotinoyl-5'-AMP, which biotinylates proximal
149 lysines within 20 nm [35]. By comparing relative biotinylation by BioID2 fused to either $G\alpha_i$
150 WT or $G\alpha_i$ QL, we revealed the activated $G\alpha_i$ proximity interactome. Here, we applied
151 this approach to probe the relative interactomes of $G\alpha_{i1}$ and $G\alpha_{i2}$.

152 Briefly, HA-$G\alpha_{i1}$ Q204L-BioID2 ($G\alpha_{i1}$ QL-BioID), HA-$G\alpha_{i2}$-BioID2 ($G\alpha_{i2}$-BioID),
153 and HA-$G\alpha_{i2}$ Q205L-BioID2 ($G\alpha_{i2}$ QL-BioID) were transiently transfected into HT1080
154 fibrosarcoma cells and incubated with biotin to allow labeling of proximal proteins by
155 $G\alpha_i$-BioID. After 24 hours of protein expression and biotin labeling, cells were lysed,
156 biotinylated proteins were captured with streptavidin beads, and labeled with isobaric
157 tandem mass tag (TMT) labels. Samples from all experimental groups were then
158 analyzed via LC MS/MS (Fig. 2A). Proteins statistically significantly enriched in QL vs
159 WT samples are considered proximal interactors. Volcano plots were generated for all
160 the proteins identified with the statistical cutoffs for significance from two different

161 comparisons, $G\alpha_{i1}$ QL/$G\alpha_{i2}$ WT (Fig. 2B top panel) and $G\alpha_{i2}$ QL/$G\alpha_{i2}$ WT (Fig. 2B
162 bottom panel). We assumed that the $G\alpha_i$ WT interactions would be similar between the
163 two subtypes thus $G\alpha_{i2}$ was used as a baseline for both plots. Validation of this
164 assumption is discussed below.

165 The identities and fold QL/WT enrichment levels for many hits for active $G\alpha_{i1}$-
166 BioID were consistent with those found in our previous screen [29]. Notably, there are no
167 significant observable differences in identity of most of the proteins enriched for
168 interaction with active $G\alpha_{i1}$ QL-BioID vs $G\alpha_{i2}$ QL-BioID. However, the number of proteins
169 identified that reached statistical significance [-log(abundance ratio p-value) ≥ 2.0] were
170 markedly fewer in $G\alpha_{i2}$ QL-BioID2 samples than in $G\alpha_{i1}$ QL-BioID2 samples. This is
171 largely because the $G\alpha_{i2}$ QL-BioID2 / $G\alpha_{i2}$ WT-BioID2 fold enrichment was generally
172 lower than for $G\alpha_{i1}$ QL BioID2. These data indicate a difference in overall signaling
173 activity of $G\alpha_{i1}$-GTP compared to $G\alpha_{i2}$-GTP.

174 To confirm that these observations are not an artifact of the mass spectrometry
175 analysis and that using $G\alpha_{i2}$ WT as a baseline in both plots is valid, verification assays
176 were performed with selected "hits" from the mass spectrometry that showed significant
177 differences between $G\alpha_{i1}$ QL and $G\alpha_{i2}$ QL engagement. Epitope-tagged mammalian
178 expression constructs were transiently co-expressed in HEK293 cells with either $G\alpha_{i1}$-
179 BioID, $G\alpha_{i1}$ QL-BioID2, $G\alpha_{i2}$-BioID2, $G\alpha_{i2}$ QL-BioID2, or membrane-targeted BioID2
180 (BioID2-CAAX). Exogenous biotin was added for 24 hours, followed by a lysis and
181 streptavidin bead purification. Captured biotinylated protein samples were run on SDS-
182 PAGE and analyzed for pulldown via western blotting using antibodies against the
183 respective affinity tags for the target proteins.

184 Proteins selected for analysis included several targets that were found in our
185 previous report [29] and represent diverse signaling pathways: PDZ-RhoGEF, α-Parvin
186 (Parvin), Vimentin, Ribosomal protein S6 Kinase A1 (RSK1), Neurofibromin 1 (NF1),
187 and Ras p21 protein activator 2 (RASA2). Proteins including NF1, PRG, and Parvin
188 showed selective enrichment in $G\alpha_{i1}$ QL/WT over $G\alpha_{i2}$ QL/WT (Fig. 2C, lanes 3-6).
189 Vimentin and RASA2 showed only a slight preference for interaction with $G\alpha_{i1}$ QL-BioID
190 over $G\alpha_{i2}$ QL-BioID, while RSK1 did not preferentially interact with either $G\alpha_{i1}$ QL-BioID
191 or $G\alpha_{i2}$ QL-BioID over the WT-BioID variants. These results indicate that many of the
192 proximal interactors found in the proteomic screen are reproducible in an orthogonal
193 assay and are suitable for further analysis in their relationship to $G\alpha_i$. Importantly, the
194 results confirm that nucleotide-dependent interaction with these targets by $G\alpha_{i2}$ is
195 weaker than for $G\alpha_{i1}$.

196 **Substitution of the $G\alpha_{i1}$ helical domain (HD) into $G\alpha_{i2}$ is sufficient to confer**
197 **activation of PRG and enhances interactions with other targets.**

198 To understand the molecular determinants that drive specificity of activation of
199 PRG by $G\alpha_{i1}$, and perhaps by extension other targets, we mapped the amino acid
200 differences between the $G\alpha_i$ subfamily onto a crystal structure of $G\alpha_{i1}$ bound to a GTP
201 analogue, GPPNHP (PDB 1CIP). We previously reported that $G\alpha_{i3}$ activates PRG, so
202 we highlighted amino acids homologous between $G\alpha_{i1}$ and $G\alpha_{i3}$ but different from $G\alpha_{i2}$
203 (33 residues) (Fig. 3A). The helical domain (HD) of $G\alpha_i$ shows the region of greatest
204 divergence between $G\alpha_i$ subtypes (Figs. 3A and 4A), containing 21 of the differences
205 between $G\alpha_{i1}$/$G\alpha_{i3}$ and $G\alpha_{i2}$. As an initial approach, we substituted the entire HD of $G\alpha_{i1}$
206 (residues 62-167) into the corresponding position in $G\alpha_{i2}$, resulting in the chimeric $G\alpha_i$

207 protein $G\alpha_{i2}$-1HD (Fig. 3B). This chimera is expressed in HEK293 cells and functionally
208 inhibits forskolin-dependent cAMP generation by adenylyl cyclase (Fig. S1A and B).
209 $G\alpha_{i2}$-1HD or $G\alpha_{i2}$-1HD Q205L (QL) were then transfected into HEK293 cells in the SRE-
210 luciferase reporter assay to examine their ability to activate PRG. Strikingly, $G\alpha_{i2}$-1HD
211 QL expression results in strong activation of PRG as compared to $G\alpha_{i2}$ QL (Fig. 3C),
212 indicating that the HD of $G\alpha_{i1}$, when substituted into $G\alpha_{i2}$, is sufficient to confer
213 nucleotide-dependent activation of PRG.

214 To try to identify structural elements within the $G\alpha_{i1}$ HD that confer PRG
215 activation, the HD was subdivided into three segments consisting of 1) The Gα αA helix,
216 2) αB – αC helices, and 3) αD – αE helices. Each of these subdivisions of the $G\alpha_{i1}$ HD
217 were then substituted into their cognate positions in $G\alpha_{i2}$ (Fig. 3B). Neither the αA helix
218 nor the αB-αC helix subdivisions of $G\alpha_{i1}$, when substituted into $G\alpha_{i2}$, activate PRG in
219 cells more than $G\alpha_{i2}$ Q205L (Fig. 3D), but inhibited cAMP generation by adenylyl
220 cyclase (Fig. S1C). The αD-αE substitution was deficient in the cAMP inhibition assay
221 and could not be analyzed. These data suggest that $G\alpha_{i1}$-mediated activation of PRG
222 relies on some intrinsic property of the intact $G\alpha_{i1}$ HD rather than one residue or a
223 subset of residues within the $G\alpha_{i1}$ HD. It is possible that the $G\alpha_{i1}$ HD participates in
224 direct binding interactions with PRG but may also confer specificity through interactions
225 with of some component of the RLD in $G\alpha_{i}$.

226 The striking increase in PRG activation observed with substitution of the $G\alpha_{i1}$ HD
227 into $G\alpha_{i2}$ prompted us to test the interaction of these $G\alpha_{i2}$ variants with other protein
228 targets from the BioID proximity labeling screen. We tested multiple targets for
229 activation-dependent labeling using the proximity labeling-dependent western blotting

230 assay with the WT and QL versions of $G\alpha_{i1}$, $G\alpha_{i2}$ and $G\alpha_{i2}$-1HD (Fig. 2C lanes 7,8,
231 S1E). Substitution of the $G\alpha_{i1}$ HD into $G\alpha_{i2}$ partially rescues the QL-dependent labeling
232 of some of these targets. Parvin shows the most striking rescue while NF1, PRG and
233 vimentin show some degree of rescue. RASA2 which does not show a preference for
234 $G\alpha_{i1}$ vs. $G\alpha_{i2}$ is not affected by the HD substitution. These data support the idea that the
235 structural differences conferred by the HD of the $G\alpha_{i}$ subunits are important for
236 differences in general target engagement beyond PRG.

237 **Residue A230 in $G\alpha_{i2}$ controls PRG activation and leads to enhanced proximity**
238 **interactome engagement**

239 Since we could not identify individual residues in HD that could confer PRG
240 activation we hypothesized that the HD could be influencing contacts in other regions of
241 Gα. In an existing co-crystal structure of $G\alpha_{13}$ bound to the rgRGS domain of PRG [36],
242 amino acids in the N-terminal portion of the PRG RGS domain bind at the $G\alpha_{13}$ HD-RLD
243 domain interface. We hypothesized that this paradigm may extend to PRG interactions
244 with $G\alpha_{i1}$ as well where the HD may cooperate with the Ras like domain to confer
245 interactions with PRG. Based on this idea we individually substituted non-conserved
246 residues (amino acids conserved between $G\alpha_{i1}$ and $G\alpha_{i3}$ but different in $G\alpha_{i2}$, starred in
247 Fig. 4A) from the $G\alpha_{i1}$ RLD into $G\alpha_{i2}$ and determined if they confer activation of PRG.
248 The majority of the mutations either had no effect or reduced activation, however,
249 substitution of $G\alpha_{i2}$ A230$^{s4h3.3}$ with Asp enables $G\alpha_{i2}$(A230D) QL to activate PRG (Fig.
250 4B, Fig. S2A), while the reverse substitution of D229 to Ala in $G\alpha_{i1}$ blunts PRG
251 activation (Fig. 4C). The $G\alpha_{i2}$ A230D substitution also confers the ability to interact with
252 PRG in a nucleotide-dependent manner in the NanoBiT complementation assay in (Fig.

253 4D, Fig. S2B). We chose two of the other targets that show differential $G\alpha_{i1}$ and $G\alpha_{i2}$
254 engagement in the proximity labeling western blot assay, NF1 and Parvin, and
255 performed the same assay comparing the QL versions of $G\alpha_{i1}$-BioID2, $G\alpha_{i2}$-BioID2 and
256 $G\alpha_{i2}$ A230D-BioID2 (Fig. 4E, Fig. S2C). The A230D substitution enhances the
257 engagement of $G\alpha_{i2}$ with these other targets. These data support the idea that the
258 structural differences conferred by either the HD, or A230$G\alpha_{i2}$/D229$G\alpha_{i1}^{s4h3.3}$, of the $G\alpha_i$
259 subunits are important for differences in general target engagement beyond PRG.
260 Additionally, the observation that these substitutions restore interactions previously
261 identified in a $G\alpha_{i1}$ BioID proximity labeling screen provides further evidence that these
262 are in fact bona fide $G\alpha_i$ interaction targets that remain to be further characterized
263 physiologically.

264 **$G\alpha_{i1}$ and $G\alpha_{i2}$ sample distinct conformations**

265 Examination of the static three-dimensional structure of $G\alpha_{i1}$ does not clearly
266 indicate why substitution at the D229/A230$^{s4h3.3}$ position, or substitution of the $G\alpha_{i1}$ HD,
267 would impact binding and/or activation of target proteins. This amino acid is near the
268 GTP binding site but is not involved in interactions with the nucleotide, and the closest
269 residue in the HD is 9Å away (Fig. 5A and B). To capture potential interactions that are
270 not observable in the crystal structures, we performed molecular dynamics (MD)
271 simulations with GTP-bound $G\alpha_{i1}$ and $G\alpha_{i2}$. We used the crystal structure of $G\alpha_i$ (PDB
272 ID:1CIP) as a starting structure for $G\alpha_{i1}$ and generated a homology model of $G\alpha_{i2}$ using
273 this structure as a template. MD simulations were run for each system totaling to 5µs.
274 Principal component analysis was used to characterize the dominant motions in $G\alpha_{i1}$
275 and $G\alpha_{i2}$. Principal Component 1 (PC1) in both proteins is rotation of the HD and RLD

276 relative to one another (Movie S1 and 3). Principal Component 2 (PC2) is a domain
277 "opening" motion where the HD opens relative to the RLD via the interdomain hinge
278 region (Movie S2 and 4). We projected all the snapshots from MD simulations on these
279 two principal components as shown in Fig. 5C. It is evident from Fig. 5C (top panel)
280 that $G\alpha_{i1}$ and $G\alpha_{i2}$ sample distinct conformation clusters in these principal component
281 coordinates. MD simulations show that even when bound to GTP, there is some degree
282 of domain opening is possible in both $G\alpha_{i1}$ and $G\alpha_{i2}$ but the domain opening is more
283 pronounced in $G\alpha_{i2}$ compared to $G\alpha_{i1}$. When these simulations were done for the
284 mutants $G\alpha_{i1}$ (D229A) the RLD-HD domain opening moved closer to that of $G\alpha_{i2}$.
285 Similarly, with the A230D substitution in $G\alpha_{i2}$, moves closer to that of $G\alpha_{i1}$ in the RLD-
286 HD domain opening coordinate (Fig. 5C bottom panel).

287 To understand the inter-residue interactions responsible for the differences in
288 domain opening between these G protein subtypes, we analyzed the residues that
289 make the interdomain contacts in the interface in all the MD snapshots. We observed
290 differential interactions between residues in Switch III and the αD-αE region of the HD in
291 $G\alpha_{i1}$ compared to $G\alpha_{i2}$ (Fig. 5D). In $G\alpha_{i1,}$ two key residues in the HD are involved in an
292 interaction network at the HD-RLD interface, $Q147^{hdhe.2}$ and $R144^{HD.11}$. In our
293 simulations during dynamic rotation of the HD-RLD interface, $R144^{HD.11}$ dynamically
294 interacts with residues $D229^{s4h3.3}$, $D231^{s4h3.5}$, $L232^{s4h3.6}$, and $S228^{s4h3.2}$ in the Switch III
295 region of the RLD, interactions that are not evident in the crystal structure (Fig. 5E left).
296 These interactions are largely absent in $G\alpha_{i2}$ (Fig. 5E mid). In $G\alpha_{i2}$, the cognate residue
297 for $G\alpha_{i1}$ D229 is A230, and substitution of A230 with D partially restores many of the
298 interdomain residue interactions with Switch III that are absent in $G\alpha_{i2}$ relative to $G\alpha_{i1}$

299 (Fig. 5E right). Similarly, HD residue Q147$^{hdhe.2}$ interacts more frequently with A235$^{s4h3.9}$,
300 R242$^{H3.1}$, and V233$^{s4h3.7}$ in $G\alpha_{i1}$ than the cognate interactions in $G\alpha_{i2}$. When $G\alpha_{i2}$
301 A230$^{s4h3.3}$ is substituted with D interactions between Q148$^{hdhe.2}$ and V234$^{s4h3.7}$ are
302 strengthened, with other contacts are largely unaffected. This supports the idea that
303 $G\alpha_{i1}$ D229 stabilizes a network of interactions between the HD and RLD-Switch III that
304 are lost in $G\alpha_{i2}$ (Fig. 5D.

305 **Bayesian network models show that $G\alpha_{i2}$ A230D mimics $G\alpha_{i1}$ in RLD-HD**
306 **interactions**

307 As another approach, a fingerprint matrix of Switch III-HD residue contacts was
308 constructed using data from the simulations. Bayesian Network Analysis was performed
309 on this matrix, yielding a full Bayesian network (shown in Fig. S3 of Supporting
310 Information) for these contacts in $G\alpha_{i1}$ and $G\alpha_{i2}$ and their mutants. Each node in this
311 network model represents a residue interaction pair between RLD and HD. Nodes were
312 then ranked by strength to understand their cooperativity ranking within the network.
313 This analysis shows that interactions between D229$^{s4h3.3}$ in the RLD and R144$^{HD.11}$ in
314 the HD forms the core of a cooperativity network involving multiple contacts in Switch III
315 (Fig. 5F, left panel). This interaction network is disrupted in $G\alpha_{i2}$ where the D229
316 cognate residue is alanine ($G\alpha_{i2}$ A230) which cannot interact with the positively charged
317 arginine ($G\alpha_{i2}$ R145$^{HD.11}$) (Fig. 5F, center panel). Substitution of A230 with D in $G\alpha_{i2}$
318 restores a cooperative interaction network with Switch III (Fig.5F, right panel). This
319 analysis supports the idea that in GTP-bound $G\alpha_{i1}$, D229 at the base of Switch III forms
320 an important contact with R144 in the HD that is not observed in crystal structures of
321 $G\alpha_{i1}$. This interaction supports a network of additional interactions between the HD and

322 multiple amino acids in Switch III that constrain the conformation of Switch III. This
323 network does not form in $G\alpha_{i2}$, likely permitting Switch III to adopt conformations other
324 than that seen in $G\alpha_{i1}$, leading to lower-efficacy interactions with effectors that require
325 Switch III for activation.

326

327

328 **PRG stimulation is dependent on interdomain stabilization of $G\alpha_i$ Switch III**

329 The simulation data indicate that an ionic interaction between D229 in the RLD
330 and R144 in the HD centers an interaction network that controls the conformation of
331 Switch III. Based on this we predicted that mutation of R144 to disrupt this interaction
332 would reduce PRG activation by $G\alpha_{i1}$. $G\alpha_{i1}$ R144A reduces nucleotide-dependent PRG
333 activation in cells, similar to that of $G\alpha_{i1}$ D229A. When alanine is substituted for both
334 D229 and R144, the same reduction is observed (Fig. 6A). Alanine substitution of
335 cognate residue R145 in $G\alpha_{i2}$ does not alter nucleotide-dependent PRG activation, but
336 completely abolishes activation of PRG conferred by A230D (Fig. 6B). These
337 experiments show that the D229-R144 interaction contributes to the ability of $G\alpha_{i1}$ to
338 activate PRG, and the ability to activate PRG conferred to $G\alpha_{i2}$ by the A230D
339 substitution is entirely dependent on the interdomain D230-R145 interaction.

340 In the Ras-like domain are the switch regions including the Switch III loop. Switch
341 III is critical for communication to the HD across the domain interface, and affects
342 multiple aspects of Gα protein function, including effector recognition [37,38] and receptor-
343 mediated activation [39]. In the cocrystal structure of $G\alpha_{13}$ and PRG, Switch III makes

344 multiple contacts with PRG. To test involvement of Switch III in $G\alpha_i$-dependent PRG
345 activation, we substituted $G\alpha_{i1}$ Switch III residues D231 – A235 (DLVLA) to cognate $G\alpha_s$
346 residues N254 – R258 (NMVIR) ($G\alpha_{i1}$ SW3αS). $G\alpha_{i1}$ SW3αS QL poorly activated PRG
347 compared to $G\alpha_{i1}$ QL in the SRE luciferase assay (Figs. 7A and B). To confirm that $G\alpha_{i1}$
348 SW3αS retains activity $G\alpha_{i1}$SW3αS was purified and compared with $G\alpha_{i1}$ and $G\alpha_{i2}$ for
349 its ability to inhibit $G\alpha_s$-stimulated adenylate cyclase. All three proteins were able to
350 equally inhibit AC demonstrating that the $G\alpha_{i1}$SW3αS chimera is functional (Fig. 7C).
351 The loss-of-function mutations in Switch III along with the gain-of-function phenotype
352 achieved by substitution of either $G\alpha_{i1}$ RLD elements or HD elements provide evidence
353 of cooperation between the RLD and HD stabilizing Switch III in a conformation needed
354 for $G\alpha_i$-mediated activation of PRG and other targets, but not inhibition of AC (Fig. 7D).
355 This stabilization is lost in $G\alpha_{i2}$.

356
357
358
359
360
361
362
363
364
365
366

367

368

369

370

371

372

373

374 **Discussion**

375 In this study, we provide evidence that $G\alpha_i$-effector interactions are dependent on
376 the strength and frequency of interaction between Switch III residues and the HD in the
377 GTP bound state, and that these interactions differ between $G\alpha_i$ subtypes. The data
378 show that $G\alpha_{i2}$ has fewer interdomain residue contacts, leading to weaker interactions
379 between Switch III in the RLD and HD. Interruption of these contacts limits the ability of
380 $G\alpha_i$ to activate PRG. It is likely that stabilization of Switch III is central to this mechanism
381 because Switch III conformational changes are dependent on the nucleotide binding
382 state (GTP vs. GDP) while the conformation of the HD is generally not altered upon
383 GTP binding. While we focused on PRG stimulation as a functional indicator of $G\alpha_i$
384 specificity, the $G\alpha_i$-BioID proximity labeling experiments demonstrate that there are
385 global differences in GTP-dependent interactions between $G\alpha_i$ subtypes and several
386 novel targets, and that these differences depend on the same substitutions of residues
387 from $G\alpha_{i1}$ into $G\alpha_{i2}$ that conferred specificity for PRG activation. This result indicates
388 stabilization of interdomain interactions in the GTP state may play an unappreciated role

389 in the downstream signaling function of $G\alpha_i$ subunits, and a major role in differentiating
390 $G\alpha_i$ subtype function.

391 The involvement of the $G\alpha_{i1}$ D229-R144 interaction and other additional
392 interdomain contacts in stabilization of Switch III and effector interactions are supported
393 by multiple key results. First, computational simulations show a dynamic interaction
394 landscape where single substitutions affect the strength of other regional contacts.
395 Second, substitution of either the $G\alpha_{i1}$ HD or A230D into $G\alpha_{i2}$ results in increased, GTP-
396 dependent interaction with PRG and other protein targets compared to $G\alpha_{i2}$ QL. Third,
397 the effects of A230D in the RLD are completely abrogated if R145 in the HD is changed
398 to alanine, strongly supporting the idea that this interdomain linkage is key to stabilizing
399 the interface and Switch III such that it can interact with targets.

400 Position s4h3.3 ($G\alpha_{i1}$ D229 and $G\alpha_{i2}$ A230) is unique for the $G\alpha_i$ subfamily in that
401 the residue is different for each Gα family but is conserved within each family except
402 $G\alpha_i$. Amino acids at this position for each family include Ser in $G\alpha_s$, Gly in $G\alpha_o$ and $G\alpha_z$,
403 Ala in $G\alpha_T$, and Glu in $G\alpha_{q/11}$ and $G\alpha_{12/13}$ (Fig. S5). A similar ionic lock mechanism for
404 stabilization of Switch III through interdomain interactions is likely conserved in the
405 $G\alpha_{q/11}$ family and also $G\alpha_{13}$, as $G\alpha_{i1}$ R144$^{HD.11}$ is conserved in these G proteins and
406 could interact in a similar way with Glu at s4h3.3 in Switch III. Despite the similarities to
407 other Gα subunits at these positions, the $G\alpha_i$ subfamily seems unique in its intra-family
408 effector specificity achieved by differentiation at s4h3.3 resulting in the presence or
409 absence of the ionic lock.

410 RLD-HD interactions have classically been understood to be a regulator of
411 nucleotide exchange [12,40-45], with mutations at the interface intended to disrupt

412 interactions leading to higher rates of GDP dissociation [12]. Specifically, mutation of
413 residue R144 in $G\alpha_{i1}$ to an alanine is known to significantly increase the rate of GTPγS
414 binding, presumably through the breaking of an interdomain interaction with L232 [12]. In
415 $G\alpha_s$, substitution of residues in the Switch III loop to those of $G\alpha_{i2}$ disrupt the ability of
416 $G\alpha_s$ to bind GTP in response receptor activation, but retains the ability to activate AC in
417 response to GTPγS activation. Activation can then be restored by additionally
418 substituting the $G\alpha_s$ HD with $G\alpha_{i2}$ residues [39,46], demonstrating the importance of Gα
419 isoform-specific interdomain communication for receptor dependent G protein
420 activation.

421 Co-crystal structures of Gα subunits in each family have shown all non-RGS
422 effectors binding to a common cleft between the α2 (Switch II) and α3 helices with no
423 apparent direct involvement of Switch III [36,47-51]. On the other hand, mutagenic analysis
424 $G\alpha_q$-GRK2 interactions revealed involvement of both the HD and Switch III [52], an
425 interaction not evident in the co-crystal structure of $G\alpha_q$ with GRK2. As another
426 example, $G\alpha_{T1}$ binding to the autoinhibitory γ subunit of cGMP phosphodiesterase
427 (PDEγ) is dependent on the presence of the HD [53], however the binding site of PDEγ is
428 not in the HD but rather in the α2-α3 cleft [51]. Crucially, mutation of a Switch III Glu to
429 Leu abolishes PDE activation by $G\alpha_T$, with no effects on nucleotide binding or hydrolysis
430 [37]. A recent cryo-EM structure of the full cGMP PDE6 αβγ complex with transducin
431 revealed the binding of PDEγ to the outer edge of the Switch III loop as well as the
432 previously solved site in the α2-α3 cleft in $G\alpha_T$-GTP [54]. Thus, there is evidence for
433 involvement of Switch III in effector engagement and our analysis reveals how two

434 proteins with identical Switch III residues can have differences in target engagement
435 efficacy.

436 While it remains untested how the lower efficacy of target engagement by $G\alpha_{i2}$
437 relative to $G\alpha_{i1}$ directly leads to distinct physiological roles, our findings are consistent
438 with the notion that $G\alpha_{i2}$ may in some situations act primarily to regulate AC and act as
439 a scaffold and switch for Gβγ signaling, whereas $G\alpha_{i1}$ or $G\alpha_{i3}$ may perform these
440 functions in addition to signaling to various $G\alpha_i$-specific effectors. This is consistent with
441 known roles for $G\alpha_{i2}$ and $G\alpha_{i3}$-mediated signaling events in neutrophils, where $G\alpha_{i2}$
442 activation promotes cell arrest while and $G\alpha_{i3}$ promotes migratory phenotypes [27].
443 Eosinophils from $G\alpha_{i2}$ whole-body knockout mice display enhanced chemotactic
444 responses *in vitro* [55]. The effects of activation of $G\alpha_{i2}$ on neutrophil arrest in cells
445 lacking $G\alpha_{i3}$ are similar to those found by Gβγ activation alone [56]. The physiological
446 situation is likely to be more complex and this model cannot fully explain physiological
447 specificity. For example, in murine atria, GIRK channel activity is differentially regulated
448 by $G\alpha_{i2}$ and $G\alpha_{i1}$/$G\alpha_{i3}$. Deletion of $G\alpha_{i2}$ increases Gβγ-mediated basal and agonist-
449 induced GIRK currents, while dual knockout of $G\alpha_{i1}$ and $G\alpha_{i3}$, which are known to bind
450 and regulate GIRK, ablates basal and muscarinic agonist-induced GIRK activity [57].
451 Nevertheless, it is probable that regulation of interdomain dynamics through the
452 intramolecular interactions we defined play a significant role in physiological specificity.

453 In conclusion, we describe here a previously unknown mechanism of effector
454 specificity between $G\alpha_i$ subtypes. Switch III is stabilized by an interdomain interaction
455 network with αD-αE residues in the helical domain, due in part to rearrangement of one
456 non-conserved $G\alpha_i$ Switch III aspartate that contacts a conserved arginine. This

457 stabilization of Switch III not only confers specificity for activation of $G\alpha_{i1/3}$ effector PDZ-
458 RhoGEF, but for interaction with an array of additional protein targets, shedding light on
459 a fundamental mystery of functional redundancy among this highly similar Gα protein
460 family.

461
462
463
464
465
466
467
468
469

470 **Methods**

471 **Plasmid cDNA constructs**
472
473 BioID2 fused N-terminally with c-Myc tag and C-terminally with mVenus, followed by
474 CaaX PM targeting motif (KKKKKKSKTKCVIM, derived from the C terminus of KRas),
475 was a gift from S. Malik of the University of Rochester. C-terminally c-Myc–tagged full-
476 length PRG cDNA construct in mammalian expression vector was a gift from J. Tesmer
477 of Purdue University. The following plasmids were obtained from Addgene: mEmerald-
478 parvin-C-14 (#54214), EGFP-vimentin-7 (#56439), HA-$G\alpha_i$-BioID2 plasmids in
479 pcDNA3.1+ were constructed as described previously [29].
480
481 All Gα clones in pcDNA3.1+ were obtained from the cDNA Resource Center. The
482 sequences of the clones are available upon request.
483
484 All mutagenesis to $G\alpha_i$ DNA constructs was accomplished using reagents, protocols,
485 and guidelines from New England Biolabs Q5® Site-Directed Mutagenesis Kit
486 (E0554S). Gαi2-1HD, all $G\alpha_{i1}$ HD subdivision constructs, and $G\alpha_i$ N- and C-terminal
487 substitutions were generated using reagents, protocols, and guidelines from New
488 England Biolabs HiFi DNA Assembly Master Mix (E2621) and Cloning Kit (E5520).
489
490 In $G\alpha_{i1}$, a FLAG epitope (DYKDDDDK) was inserted between Ala 121 and Glu 122 and
491 flanked by a flexible linker (SGGGGS) on both sides of the insert. The FLAG epitope in

492 $G\alpha_{i2}$ was inserted in the same manner with the same linkers at the analogous position
493 as $G\alpha_{i1}$, between Asp 122 and Asp 123.
494
495 $G\alpha_{i1}$ SW3αS-FLAG was generated using Q5 mutagenesis by substituting $G\alpha_s$ residues
496 N254 – R258 (NMVIR) into their cognate position in $G\alpha_{i1}$, D231 – A235 (DLVLA) in
497 FLAG-tagged $G\alpha_{i1}$.
498
499 SmBiT-PRG was generated by inserting the SmBiT sequence (VTGYRLFEEIL) followed
500 by a flexible linker (SGGGGS) onto the N-terminus of cMyc-PRG (cMyc: EQKLISEEDL),
501 resulting in SmBiT-Linker-cMyc-PRG.
502
503 **Cell Culture**
504
505 A293 and HT1080 cells were obtained from the American Type Culture Collection.
506 A293 and HT1080 cells were grown supplemented in DMEM (Dulbecco's modified
507 Eagle medium) with 10% fetal bovine serum (FBS) (10437028, Gibco) and 100 U of
508 penicillin/streptomycin (15140122, Gibco) at 37°C with 5% CO2. Trypsin-EDTA
509 (25200056, Gibco) was used for cell passage.
510
511 **Reagents**
512
513 The following primary and secondary antibodies were used: $G\alpha_{i1/2}$ (anti-sera) [58], c-Myc
514 (13-2500, Invitrogen), GFP (A11122, Invitrogen), HA (C29F4, Cell Signaling), FLAG
515 (PA1-984B, Invitrogen). Streptavidin-IRDye800 was from LI-COR (925-32230). Primary
516 antibodies were diluted in 3% bovine serum albumin (BSA) and 0.1% sodium azide and
517 incubated with blots overnight at 4°C. Streptavidin-IRDye800 was incubated for 1 hour
518 at room temperature. For secondary antibodies, goat anti-rabbit DyLight 800
519 (SA535571, Invitrogen) and goat anti-mouse IRDye 800CW (926-32210, LI-COR) were
520 used at 1:10,000.
521
522 **NanoBiT Luciferase Complementation Assay**
523
524 6.0 x 10^5 HEK293A cells were seeded in poly-D-lysine coated 6-well plates (Fisher
525 FB012927). Immediately after plating, HA-Gα-LgBiT constructs and SmB-cmyc-PDZ-
526 RhoGEF were co-transfected using a 1:3 mass to volume ratio of DNA to Lipofectamine
527 2000 (Invitrogen). After 24 hours, transfection media was aspirated and cells were
528 gently washed once with 1 mL warm PBS. The PBS was discarded, 200 µL trypsin
529 solution was added, and the plate was incubated at 37°C and 5% CO_2 for 5 mins.
530 Following incubation, 800 µL of warm 1X HBSS was added to each well, and the
531 detached cells were aspirated and dispensed into new 15 mL conical tubes. Cells were
532 then pelleted by centrifugation at 250 x g for 5 mins at RT. After carefully aspirating the
533 supernatant, each pellet was resuspended in 1 mL warm HBSS, and cell number in
534 each suspension counted. Cell suspensions were centrifuged once more at 250 x g for
535 5 mins at RT and resuspended in warm 10 µM furimazine in HBSS, 1% DMSO. 5 x 10^4
536 cells were distributed to each well in a 96-well plate; samples were analyzed with six

technical replicates. The sample plate was incubated at 37°C for 15 mins, followed by a luminescence measurement in each well.

SRE-Luciferase Reporter Assay

96-well format

4.5 x 10^4 HEK293A cells were seeded in poly-D-lysine coated 96-well plates (Greiner 655983). Cells were transfected with the following plasmids and amounts per well: 25 ng SRE-Luc reporter (E134A, Promega), 75 ng $G\alpha_i$ or $G\alpha_i$ QL in pcDNA3.1+, 2.5 ng cmyc-PRG unless otherwise indicated. Minor adjustments in added DNA were made to equalize expression of $G\alpha_i$ subunits based on western blotting of Flag tagged constructs. In these cases, empty pcDNA3.1+ vector supplemented to equalize total DNA added per well. Transfection took place immediately after seeding with a 1:3 mass to volume ratio of DNA to Lipofectamine 2000 (Invitrogen). Twelve hours after transfection, the media was replaced with 75 µL of serum-free media. Twenty-four hours after transfection, 75 µL (1:1 volume) of One-Glo reagent (E6110, Promega) was added to each well and incubated for 10 min at room temperature. The luminescence signal was measured using Varioskan LUX multimode microplate reader (Thermo Fisher Scientific).

24-well format

The SRE-Luc reporter assay was also performed nearly identically in 24-well plates, which offered better well-to-well consistency for technical replicates. 1 x 10^5 HEK293A cells were seeded in poly-D-lysine coated 24-well plates. One hundred ng SRE-Luc reporter (E134A, Promega), 300 ng $G\alpha_i$ or $G\alpha_i$ QL in pcDNA3.1+, and 5 ng cmyc-PRG DNA were transfected into each well except in $G\alpha_i$ titration experiments, where reduced $G\alpha_i$ DNA was substituted with empty pcDNA3.1+. Transfection took place immediately after seeding with a 1:3 mass to volume ratio of DNA to Lipofectamine 2000 (Invitrogen). Twelve hours after transfection, the media was replaced with 250 µL of serum-free media. Twenty-four hours after transfection, 250 µL (1:1 volume) of One-Glo reagent (E6110, Promega) was added to each well and incubated for 10 min at room temperature. The luminescence signal was measured using Varioskan LUX multimode microplate reader (Thermo Fisher Scientific). We found that the fold differences in activation by $G\alpha_i$ were lower in the 24 well format but that the technical replicates were more reliable.

GloSensor cAMP Assay

582 4.5 x 10^4 HEK293A cells were seeded in poly-D-lysine coated 96-well plates (Greiner
583 655983). Cells were transfected with the following plasmids and amounts per well: 50
584 ng GloSensor -20F cAMP plasmid (E1171, Promega), 125 ng $G\alpha_i$ or $G\alpha_i$ QL in
585 pcDNA3.1+. In $G\alpha_i$ titration experiments, DNA was supplemented with empty
586 pcDNA3.1+ vector. Transfection took place immediately after seeding with a 1:3 mass
587 to volume ratio of DNA to Lipofectamine 2000 (Invitrogen). Twenty-four hours post-
588 transfection, the media was discarded and the cells were loaded with 75 µL 0.5 mg/mL
589 D-Luciferin (L2916, Sigma Aldrich) in Leibowitz's L-15 medium followed by incubating
590 for 2 hours at 37°C and 5% CO_2. Plates were removed from the incubator and
591 equilibrated at room temperature. Forskolin was then added to give a 1 mM final
592 concentration and luminescence was measured at 15 min in a plate reader.
593
594 **Western blotting**
595
596 Samples in 1X Laemmli sample buffer were resolved on 4-20% gradient Mini-
597 PROTEAN TGX gels (4561094, Bio-Rad), transferred to nitrocellulose membranes (Pall
598 66485), and stained with Ponceau S (141194, Sigma Aldrich). Membranes were
599 blocked with 3% bovine serum albumin (141194, Sigma Aldrich) in TBST (0.1% Tween-
600 20 in 20 mM Tris pH 7.5 + 150 mM NaCl) at room temperature (RT) for 30 min with
601 constant agitation. Primary antibodies were applied for 2 hours at RT or overnight at
602 4°C. After three RT washes with TBST at 5 min each, secondary antibodies were
603 applied for 1 hour. Membranes were imaged on an Odyssey Infrared Imaging System
604 (LI-COR Biosciences).
605
606 **BioID2 proximity labeling and tandem mass spectrometry analysis**
607
608 HT1080 cells at passage number up to 15 were used for proximity labeling experiments.
609 Cells were plated into 175 cm^2 flasks at a density of 5.5 × 10^6 cells per flask. The next
610 day, media was replaced with 35 mL of DMEM containing 50 µM biotin and 10% FBS.
611 Each flask was transfected with 8 µg of plasmid encoding BioID2-fused $G\alpha_i$ construct
612 and 4 µg of YFP cDNA. A total of 0.6 µL of Viromer Red (VR-01LB-00, Lipocalyx,
613 Germany) reagent was used per 2 µg of cDNA for transfection, resulting in ~80 to 85%
614 transfection efficiency. Twenty-four hours after labeling and transfection, the labeling
615 medium was decanted, cells were washed twice with 1× PBS, and harvested at 4000 x
616 g for 10 min. This step was repeated twice using 1× PBS to recover the maximum
617 number of cells. The supernatant was aspirated, and pellets were flash-frozen and
618 stored at −80°C until further use.
619
620 All stock solutions used for streptavidin pulldown were freshly prepared, except lysis
621 buffer. Low protein binding tubes (022431081, Eppendorf) were used for sample
622 preparation. Frozen pellets were lysed in 1 mL of ice-cold lysis solution (composition
623 described above) for 10 min on ice and incubated with 125 U of benzonase with end
624 over-end rotation at 4°C for 20 min. A total of 0.3% SDS was added to lysates, which
625 were incubated for another 10 min at 4°C. Lysates were centrifuged at 15,000 x g for 15
626 min. The supernatant was transferred to fresh tubes, and the total protein concentration
627 was measured using Pierce 660 nm protein assay reagent. A total of 5% of lysates,

adjusted for protein concentration, was reserved to analyze the biotinylation in inputs. The remaining lysates were incubated with 500 µL of Pierce streptavidin magnetic beads slurry per sample in an end-over-end rotator at 4°C overnight. Beads were washed twice with modRIPA buffer [modRIPA: 50 mM tris, 150 mM NaCl, 0.1% SDS, 0.5% sodium deoxycholate, and 1% Triton X-100 (final pH 7.5)] and once with four different solutions: 1 M KCl, 0.1 M Na_2CO_3, 2% SDS [in 50 mM tris (pH 7.5)], and 2 M urea [in 10 mM tris (pH 8.0)]. Beads were washed twice with 1× PBS and were flash-frozen and stored at -80°C until further processed for MS.

BioID2 proximity labeling and immunoblot analysis

1.5 x 10^6 HEK293A cells were seeded in a poly-D-lysine coated 10 cm plate. The next day, media was replaced with 10 mL DMEM +10% FBS and biotin was added to 50 µM. Cells were transfected with 3 µg of either BioID-CAAX or one of the $G\alpha_i$-BioID2-HA constructs in pcDNA3.1+, in addition to 3 µg of one of the effectors of interest (cmyc-PRG, V5-ADNP, RASA2-FLAG, mEmerald-Parvin, RSK1-HA, or GFP-Vimentin). DNA complexes were added to Lipofectamine 2000 solutions with a 1:3 mass:volume ratio (18 µL per plate). After 24 hours of expression and labeling, the medium was decanted, cells were rinsed twice with 5 mL of ice cold 1X PBS, scraped off of the plate, and pelleted at 4°C and 4000 x g for 10 min. The supernatant was aspirated and the cell pellets were flash-frozen with liquid N_2 and stored at -80°C until processed via IP.

For the IP, 500 µL ice cold modRIPA was used to resuspend cell pellets. Lysis using benzonase and SDS proceeded as above. Lysates were centrifuged for 15,000 x g for 15 min at 4°C, and protein concentration was measured using Pierce 660 nm protein assay reagent. After equalizing for protein concentration, 20 µL of each sample volume was retained as an input sample. Five hundred µL of each equalized sample was added to 170 µL of Pierce streptavidin magnetic bead slurry and rotated end-over-end at 4°C for at least 2 hours to capture biotinylated proteins. Beads were washed three times with ice cold modRIPA and once more with cold 1X PBS. Beads were then resuspended in 100 µL 1X PBS, and 4X Laemmli sample buffer was added to 1X final concentration. Beads were boiled for 10 min at 95°C, and the supernatant was analyzed by western blot using anti-HA (1:2000) for $G\alpha_i$-BioID2-HA and the corresponding antibody for each protein of interest [cmyc-PRG – anti-cmyc (1:2000), V5-ADNP – anti-V5 (1:1000), RASA2-FLAG – anti-FLAG (1:1000), mEmerald-Parvin – anti-GFP (1:1000), RSK1-HA – anti-HA (1:2000), or GFP-Vimentin – anti-GFP (1:1000)].

Protein digestion and TMT labeling

On-bead digestion followed by liquid chromatography–tandem MS (LC-MS/MS) analysis was performed at the MS-based Proteomics Resource Facility of the Department of Pathology at the University of Michigan. Samples were reduced (10 mM dithiothreitol in 0.1 M triethylammonium bicarbonate (TEAB) at 45°C for 30 min), alkylated (55 mM 2-chloroacetamide at room temperature for 30 min in the dark), and subsequently digested using a 1:25 ratio of trypsin (V5113, Promega):protein at 37°C with constant mixing. A total of 0.2% trifluoroacetic acid was added to stop the proteolysis, and

674 peptides were desalted using a Sep-Pak C18 cartridge (WAT036945, Waters Corp).
675 The desalted peptides were dried in a vacufuge and reconstituted in 100 µl of 0.1 M
676 TEAB. A TMT10plex Isobaric Label Reagent Set plus TMT11-131C Label Reagent kit
677 (A37725, Thermo Fisher Scientific) was used to label each sample per the
678 manufacturer's protocol. The samples were labeled with TMT 11-plex reagents at room
679 temperature for 1 hour. The reaction was quenched by adding 8 µL of 5%
680 hydroxylamine for 15 min and dried. An offline fractionation of the combined sample into
681 eight fractions was performed using a high pH reverse-phase peptide fractionation kit,
682 as per the manufacturer's protocol (84868, Pierce). Fractions were dried and
683 reconstituted in 12 µL of 0.1% formic acid/2% acetonitrile for LC-MS/MS analysis.
684
685 **LC-MS analysis**
686
687 An Orbitrap Fusion (Thermo Fisher Scientific) and RSLC Ultimate 3000 nano-UPLC
688 (Dionex) were used to acquire the data. For superior quantitation accuracy, we used
689 multinotch-MS3 [59]. Two microliters of each fraction was resolved on a nanocapillary
690 reverse-phase column (75 µm internal diameter by 50 cm; PepMap RSLC C18 column,
691 Thermo Fisher Scientific) at a flowrate of 300 nL/min using 0.1% formic acid/acetonitrile
692 gradient system (2 to 22% acetonitrile in 110 min; 22 to 40% acetonitrile in 25 min; 6-
693 min wash at 90% acetonitrile; 25 min re-equilibration) and directly sprayed onto the
694 Orbitrap Fusion using EasySpray source (Thermo Fisher Scientific). The mass
695 spectrometer was set to collect one MS1 scan [Orbitrap; 120,000 resolution; AGC target
696 2 × 105; max IT (maximum ionization time) 50 ms] and data-dependent, "Top Speed" (3
697 s) MS2 scans [collision-induced dissociation; ion trap; NCE (normalized collision
698 energy) 35; AGC (automatic gain control) 5 × 103; max IT 100 ms]. For multinotch-MS3,
699 the top 10 precursors from each MS2 were fragmented by high energy collisional
700 dissociation (HCD), followed by Orbitrap analysis (NCE 55; 60,000 resolution; AGC 5 ×
701 104; max IT 120 ms, 100 to 500 mass/charge ratio scan range).
702
703 **Purification of $G\alpha_i$ subunits**
704
705 C-terminally hexahistidine tagged $G\alpha_i$ subunits and chimeras were co-expressed with
706 *N*-myristoyltransferase in E. coli as previously described [60]. Proteins were purified using
707 Ni-NTA chromatography using a gradient from 0-200 mM imidazole which resulted in
708 proteins of greater than 90% purity. Myristoylation was confirmed by analyzing
709 molecular weights on SDS-PAGE and G protein nucleotide binding activity was
710 assessed using [^{35}S]-GTPγS binding. All proteins had 20-40% nucleotide binding
711 activity.
712
713 **Adenylyl Cyclase Activity Assays**
714
715 Membranes from Sf9 cells expressing hAC6 (10 µg per reaction) were assayed for
716 adenylyl cyclase activity as described [61]. Purified and GTPγS-activated myristoylated
717 $G\alpha_{i1}$SW3αs, $G\alpha_{i1}$ and $G\alpha_{i2}$ were preincubated with membranes for 5 min on ice.
718 $G\alpha_s$·GTPγS (30 nM final) was added and preincubated for 5 min on ice prior to the start

of the assay (10 min at 30 C). Reactions were stopped with 0.2N HCL and cAMP was detected by enzyme immunoassay (Assay Designs).

Generating structural models and molecular dynamics simulations

The structural model of monomeric GTP-bound $G\alpha_{i1}$ and $G\alpha_{i2}$ protein with Mg^{2+} ion was built using the monomeric GTP bound rat $G\alpha_{I1}$ crystal structure (PDB ID: 1CIP) as template and using the homology modeling method in the Prime module of Maestro software from Schrodinger (https://www.schrodinger.com/products/maestro). The GNP present in the original crystal structure was converted to GTP using Maestro edit panel. Point mutations to generate the structures of $G\alpha_{i1}^{D229A}$ and $G\alpha_{i2}^{A230D}$ were performed using Maestro Biologics suite. The side chain packing was done for all the residues within 5Å of the mutated residue position including the mutated residues using Maestro Prime suite. All structures further underwent energy minimization using conjugate gradient method with a convergence cutoff of 0.1kcal/mol/Å. Input files for molecular dynamics simulations were generated using CHARMM-GUI [62]. Each monomeric $G\alpha_i$ protein was solvated in explicit TIP3P water molecules in a cubic box (9.0nm x 9.0nm x 9.0nm) with 0.15M of potassium chloride to mimic the physiological condition. We used GROMACS software [63] (Version 2021.3) with all-atom CHARMM36 force field [64] to perform molecular dynamics simulations. MD simulations were performed at 310°K coupled to a temperature bath with a relaxation time of 0.1ps [65]. Pressure of the systems was calculated with molecular virial and was held constant by a weak coupling to a pressure bath with a relaxation time of 0.5ps. Equilibrium bond length and geometry of water molecules were constrained using the SHAKE algorithm [66]. The short-range electrostatic and van der Waals interactions were estimated every 2fs using a charged group pair list with cutoff of 8Å between centers of geometry of charged groups. Long-range van der Waals interactions were calculated using a cutoff of 14Å and long-range electrostatic interactions were treated with the particle mesh Ewald method [67]. Temperature was kept constant at 310°K by applying the Nose-Hoover thermostat [68]. Desired pressure for all systems were achieved by using Parrinello-Rahman barostat with a pressure relaxation time of 2ps [69]. Before production runs, all system were subjected to a 5000-step steepest descent energy minimization to remove bad contacts [70]. After minimization, the systems were heated up to 310°K under constant temperature-volume ensemble (NVT). The simulations were saved every 200ps for analysis. The protein, Mg^{2+} ion, and nucleotide were subjected to positional constraints under a harmonic force constant of 1000 kJ/(mol*nm^2) during the NVT step while solvent molecules were free to move. The systems then were further equilibrated using a constant pressure ensemble (NPT), in which the force constant is applied to the protein, Mg^{2+} ion, and nucleotide were gradually reduced from 5kJ/(mol*nm^2) to zero in six steps of 5ns each. An additional 50ns of unconstraint simulation was performed, making it a total of 80ns NPT equilibration prior to production runs. We performed five production runs of 1000ns each using five different initial velocities for every system. Therefore, we had 5μs long MD trajectories for both WT and mutant systems of $G\alpha_{i1}$ and $G\alpha_{i2}$ protein.

762 **Principal Component Analysis and representative structures**

763 The last 600ns of five independent molecular dynamics simulation runs were merged
764 into one concatenated trajectory for each system. Two merged trajectories were further
765 created based on the concatenated trajectories: one contains the WT $G\alpha_{i1}$ and $G\alpha_{i2}$
766 trajectories, and the other contains all four trajectories. Principal component analysis
767 was performed on each merged trajectory using the gmx covar module of GROMACS
768 with covariance matrix of C alpha atoms of all residues. The first two principal
769 components (PC1 and PC2) of every system were extracted using gmx anaeig module
770 of GROMACS and imported into Python as a data-frame using the Pandas package.
771 Kernel density estimation maps were generated using Python Seaborn package
772 (version 0.9.0) and plotted using Python Matplotlib package.

773 **Representative structure extraction**

774 Using Get-contact data (see previous), frame numbers in $G\alpha_{i2}^{A230D}$ trajectory that have
775 contacts between R145 and D230 were recorded. The corresponding frames were
776 extracted from the trajectory using gmx trjconv module of GROMACS. The
777 representative structure of $G\alpha_{i1}$ was used as template, and the root-mean-square
778 deviation (RMSD) values of the extracted $G\alpha_{i2}^{A230D}$ frames were calculated using gmx
779 rms module: C alpha atoms were selected for both alignment and calculation. The
780 frame with the smallest RMSD value was selected as the representative structure for
781 $G\alpha_{i2}^{A230D}$ system.

782 **Calculating the fingerprints of pairwise interactions between AHD and switch III**
783 **domain of G protein**

784 The analysis of the landscape of pairwise intermolecular residue contacts between AHD
785 domain and switch III region of $G\alpha_i$ with MD simulations using the "getcontacts" python
786 script library (https://www.github.com/getcontacts). This was utilized to identify various
787 types of contacts, including salt-bridges (<4.0 Å cutoff between anion and cation atoms),
788 hydrogen bonds (<3.5 Å cutoff between hydrogen donor and acceptor atoms, <70°
789 angle between donor and acceptor), van der Waals (<2 Å difference between two
790 atoms), pi-stack contacts (<7.0 Å distance between aromatic centers of aromatic
791 residues, <30° angle between normal vectors emanating from aromatic plane of each
792 residue), and cation-pi contacts (<6.0 Å distance between cation atom and centroid of
793 aromatic rink, <60° angle between normal vector from aromatic plane to cation atom).
794 To conduct the analysis, the MD simulation trajectories were concatenated into 1μs
795 ensembles and stored as xtc coordinate files. Subsequently, water and ions were
796 stripped from the trajectory files utilized for the contact analysis, and atom selection
797 groups were matched with the relevant amino acid residues for each protein domain. In-
798 house python scripts were used to perform one-hot encoding to generate a binary
799 fingerprint for each simulation. The one-hot encoding represented the presence of a
800 contact between two residues in a particular frame with "1" and its absence with "0".

801 **Bayesian Network Analysis**

802 Binary fingerprints of residue contact pairs were analyzed to understand their
803 interdependent interactions using BNOmics, software developed for Bayesian network
804 analysis. Separate BNs were first constructed for each G protein type. Heuristic network
805 model selection search [71] was carried out with 50 random restarts, to ensure
806 convergence. Bayesian networks of contact fingerprints have residue pairs as nodes
807 and the edge weight between the nodes correlates with the dependency between them.
808 As a measure of contact pairs' connectivity, the network property of node strength was
809 used - the total sum of edge weights belonging to this node. After sorting the residue
810 pairs from highest node strength to the lowest, the top 25 percentile of them was
811 compared between different G protein types. Graphical representation of these nodes
812 and their interconnections were demonstrated using network visualization software
813 Cytoscape 3.9.1 (https://cytoscape.org/).

814

815 **Supplemental Movies**

816 Movie S1. Video of PC1 movements in GTP-bound $G\alpha_{i1}$

817 Movie S2. Video of PC2 movements in GTP-bound $G\alpha_{i1}$

818 Movie S3. Video of PC1 movements in GTP-bound $G\alpha_{i2}$

819 Movie S4. Video of PC2 movements in GTP-bound $G\alpha_{i2}$

820

821 **Author Contributions**

822 TJL performed experiments, participated in experimental design, wrote the manuscript.
823 WW performed experiments, participated in experimental design, and edited the
824 manuscript. EM performed experiments, participated in experimental design, and edited
825 the manuscript. SMV performed experiments. NC participated in experimental design.
826 SA performed experiments, YL performed experiments, CWD participated in
827 experimental design and edited the manuscript, NV participated in experimental design
828 and edited the manuscript, AVS participated in experimental design and edited the
829 manuscript.

830

831 **Research Funding**

832 AVS NIH R35GM127303, TJL AHA 826816, NV R01-GM117923 and R01-LM013876

833

References

1. Sriram, K. & Insel, P.A. G Protein-Coupled Receptors as Targets for Approved Drugs: How Many Targets and How Many Drugs? *Mol Pharmacol* **93**, 251-258 (2018).

2. Hauser, A.S., Attwood, M.M., Rask-Andersen, M., Schioth, H.B. & Gloriam, D.E. Trends in GPCR drug discovery: new agents, targets and indications. *Nat Rev Drug Discov* **16**, 829-842 (2017).

3. Gilman, A.G. G proteins: transducers of receptor-generated signals. *Annu Rev Biochem* **56**, 615-49 (1987).

4. Hepler, J.R. & Gilman, A.G. G proteins. *Trends Biochem Sci* **17**, 383-7 (1992).

5. Oldham, W.M. & Hamm, H.E. Heterotrimeric G protein activation by G-protein-coupled receptors. *Nat Rev Mol Cell Biol* **9**, 60-71 (2008).

6. Calebiro, D., Koszegi, Z., Lanoiselee, Y., Miljus, T. & O'Brien, S. G protein-coupled receptor-G protein interactions: a single-molecule perspective. *Physiol Rev* **101**, 857-906 (2021).

7. Coleman, D.E. et al. Structures of active conformations of Gi alpha 1and the mechanism of GTP hydrolysis. *Science* **265**, 1405-12 (1994).

8. Knight, K.M. et al. A universal allosteric mechanism for G protein activation. *Mol Cell* **81**, 1384-1396 e6 (2021).

9. Van Eps, N. et al. Interaction of a G protein with an activated receptor opens the interdomain interface in the alpha subunit. *Proceedings of the National Academy of Sciences* **108**, 9420-9424 (2011).

10. Chung, K.Y. et al. Conformational changes in the G protein Gs induced by the β2 adrenergic receptor. *Nature* **477**, 611-615 (2011).

11. Rasmussen, S.G.F. et al. Crystal structure of the β2 adrenergic receptor–Gs protein complex. *Nature* **477**, 549-555 (2011).

12. Remmers, A.E., Engel, C., Liu, M. & Neubig, R.R. Interdomain Interactions Regulate GDP Release from Heterotrimeric G Proteins. *Biochemistry* **38**, 13795-13800 (1999).

13. Wang, D. et al. A deep proteome and transcriptome abundance atlas of 29 healthy human tissues. in *Molecular systems biology* Vol. 15 e8503 (2019).

14. Itoh, H. et al. Presence of three distinct molecular species of Gi protein alpha subunit. Structure of rat cDNAs and human genomic DNAs. *Journal of Biological Chemistry* **263**, 6656-6664 (1988).

15. Linder, M.E., Ewald, D.A., Miller, R.J. & Gilman, A.G. Purification and characterization of Go alpha and three types of Gi alpha after expression in Escherichia coli. *Journal of Biological Chemistry* **265**, 8243-8251 (1990).

16. Taussig, R., Tang, W.J., Hepler, J.R. & Gilman, A.G. Distinct patterns of bidirectional regulation of mammalian adenylyl cyclases. *Journal of Biological Chemistry* **269**, 6093-6100 (1994).

17. Peleg, S., Varon, D., Ivanina, T., Dessauer, C.W. & Dascal, N. Gαi Controls the Gating of the G Protein-Activated K+ Channel, GIRK. *Neuron* **33**, 87-99 (2002).

18. Ivanina, T. et al. Gαi1 and Gαi3 Differentially Interact with, and Regulate, the G Protein-activated K+ Channel. *Journal of Biological Chemistry* **279**, 17260-17268 (2004).

19. Rubinstein, M., Peleg, S., Berlin, S., Brass, D. & Dascal, N. Gαi3 primes the G protein-activated K+ channels for activation by coexpressed Gβγ in intact Xenopus oocytes. *The Journal of Physiology* **581**, 17-32 (2007).

20. Rubinstein, M. et al. Divergent regulation of GIRK1 and GIRK2 subunits of the neuronal G protein gated K+ channel by GαiGDP and Gβγ. *The Journal of Physiology* **587**, 3473-3491 (2009).

21. Dizayee, S. et al. Galphai2- and Galphai3-specific regulation of voltage-dependent L-type calcium channels in cardiomyocytes. *PLoS One* **6**, e24979 (2011).

22. Cao, C. et al. Gαi1 and Gαi3 Are Required for Epidermal Growth Factor-Mediated Activation of the Akt-mTORC1 Pathway. *Science Signaling* **2**, ra17-ra17 (2009).

23. Köhler, D. et al. Gαi2- and Gαi3-Deficient Mice Display Opposite Severity of Myocardial Ischemia Reperfusion Injury. *PLOS ONE* **9**, e98325 (2014).

24. DeGeorge, B.R., Jr. et al. Targeted inhibition of cardiomyocyte Gi signaling enhances susceptibility to apoptotic cell death in response to ischemic stress. *Circulation* **117**, 1378-87 (2008).

25. Foerster, K. et al. Cardioprotection specific for the G protein Gαi2 in chronic adrenergic signaling through β2-adrenoceptors. **100**, 14475-14480 (2003).

26. Kaur, K. et al. Gαi2 signaling: friend or foe in cardiac injury and heart failure? *Naunyn Schmiedebergs Arch Pharmacol* **385**, 443-53 (2012).

27. Kuwano, Y., Adler, M., Zhang, H., Groisman, A. & Ley, K. Gαi2 and Gαi3 Differentially Regulate Arrest from Flow and Chemotaxis in Mouse Neutrophils. *The Journal of Immunology* **196**, 3828-3833 (2016).

28. Thompson, B.D. et al. Inhibition of Gαi2 Activation by Gαi3 in CXCR3-mediated Signaling. *Journal of Biological Chemistry* **282**, 9547-9555 (2007).

29. Chandan, N.R., Abraham, S., SenGupta, S., Parent, C.A. & Smrcka, A.V. A network of Gαi signaling partners is revealed by proximity labeling proteomics analysis and includes PDZ-RhoGEF. *Science Signaling* **15**, eabi9869 (2022).

30. Masters, S.B. et al. Mutations in the GTP-binding site of GSα alter stimulation of adenylyl cyclase. *Journal of Biological Chemistry* **264**, 15467-15474 (1989).

31. Graziano, M.P. & Gilman, A.G. Synthesis in Escherichia coli of GTPase-deficient mutants of Gsα. *Journal of Biological Chemistry* **264**, 15475-15482 (1989).

32. Wong, Y.H. et al. Mutant α subunits of Gi2 inhibit cyclic AMP accumulation. *Nature* **351**, 63-65 (1991).

33. Dixon, A.S. et al. NanoLuc Complementation Reporter Optimized for Accurate Measurement of Protein Interactions in Cells. *ACS Chemical Biology* **11**, 400-408 (2016).

34. Laschet, C., Dupuis, N. & Hanson, J. A dynamic and screening-compatible nanoluciferase-based complementation assay enables profiling of individual GPCR-G protein interactions. *J Biol Chem* **294**, 4079-4090 (2019).

35. Kim, D.I. et al. An improved smaller biotin ligase for BioID proximity labeling. *Mol Biol Cell* **27**, 1188-96 (2016).

36. Chen, Z., Singer, W.D., Danesh, S.M., Sternweis, P.C. & Sprang, S.R. Recognition of the activated states of Galpha13 by the rgRGS domain of PDZRhoGEF. *Structure* **16**, 1532-43 (2008).

37. Li, Q. & Cerione, R.A. Communication between Switch II and Switch III of the Transducin α Subunit Is Essential for Target Activation. *Journal of Biological Chemistry* **272**, 21673-21676 (1997).

38. Pereira, R. & Cerione, R.A. A Switch 3 Point Mutation in the α Subunit of Transducin Yields a Unique Dominant-negative Inhibitor. *Journal of Biological Chemistry* **280**, 35696-35703 (2005).

39. Grishina, G. & Berlot, C.H. Mutations at the Domain Interface of Gsα Impair Receptor-mediated Activation by Altering Receptor and Guanine Nucleotide Binding. *Journal of Biological Chemistry* **273**, 15053-15060 (1998).

40. Kim, H.R., Ahn, D., Jo, J.B. & Chung, K.Y. Effect of α-helical domain of Gi/o α subunit on GDP/GTP turnover. *Biochemical Journal* **479**, 1843-1855 (2022).

41. Jones, J.C., Jones, A.M., Temple, B.R.S. & Dohlman, H.G. Differences in intradomain and interdomain motion confer distinct activation properties to structurally similar Gα proteins. *Proceedings of the National Academy of Sciences* **109**, 7275-7279 (2012).

42. Marin, E.P. et al. The Function of Interdomain Interactions in Controlling Nucleotide Exchange Rates in Transducin. *Journal of Biological Chemistry* **276**, 23873-23880 (2001).

43. Toyama, Y. et al. Dynamic regulation of GDP binding to G proteins revealed by magnetic field-dependent NMR relaxation analyses. *Nature Communications* **8**, 14523 (2017).

44. Noel, J.P., Hamm, H.E. & Sigler, P.B. The 2.2 Å crystal structure of transducin-α complexed with GTPγS. *Nature* **366**, 654-663 (1993).

45. Codina, J. & Birnbaumer, L. Requirement for intramolecular domain interaction in activation of G protein alpha subunit by aluminum fluoride and GDP but not by GTP gamma S. *Journal of Biological Chemistry* **269**, 29339-29342 (1994).

46. Marsh, S.R., Grishina, G., Wilson, P.T. & Berlot, C.H. Receptor-Mediated Activation of Gsα: Evidence for Intramolecular Signal Transduction. *Molecular Pharmacology* **53**, 981-990 (1998).

47. Tesmer, J.J.G., Sunahara, R.K., Gilman, A.G. & Sprang, S.R. Crystal Structure of the Catalytic Domains of Adenylyl Cyclase in a Complex with Gsα-GTPγS. *Science* **278**, 1907-1916 (1997).

48. Tesmer, V.M., Kawano, T., Shankaranarayanan, A., Kozasa, T. & Tesmer, J.J.G. Snapshot of Activated G Proteins at the Membrane: The Gαq-GRK2-Gβγ; Complex. *Science* **310**, 1686-1690 (2005).

49. Lyon, A.M., Dutta, S., Boguth, C.A., Skiniotis, G. & Tesmer, J.J.G. Full-length Gαq–phospholipase C-β3 structure reveals interfaces of the C-terminal coiled-coil domain. *Nature Structural & Molecular Biology* **20**, 355-362 (2013).

50. Hajicek, N. et al. Identification of critical residues in G(alpha)13 for stimulation of p115RhoGEF activity and the structure of the G(alpha)13-p115RhoGEF regulator of G protein signaling homology (RH) domain complex. *J Biol Chem* **286**, 20625-36 (2011).

51. Slep, K.C. et al. Structural determinants for regulation of phosphodiesterase by a G protein at 2.0 Å. *Nature* **409**, 1071-1077 (2001).

52. Day, P.W. et al. Characterization of the GRK2 binding site of Galphaq. *J Biol Chem* **279**, 53643-52 (2004).

53. Liu, W. & Northup, J.K. The helical domain of a G protein alpha subunit is a regulator of its effector. *Proc Natl Acad Sci U S A* **95**, 12878-83 (1998).

54. Gao, Y. et al. Structure of the Visual Signaling Complex between Transducin and Phosphodiesterase 6. *Mol Cell* **80**, 237-245 e4 (2020).

55. Pero, R.S. et al. $G\alpha_{i2}$-mediated signaling events in the endothelium are involved in controlling leukocyte extravasation. *Proceedings of the National Academy of Sciences* **104**, 4371-4376 (2007).

56. Surve, C.R., To, J.Y., Malik, S., Kim, M. & Smrcka, A.V. Dynamic regulation of neutrophil polarity and migration by the heterotrimeric G protein subunits Galphai-GTP and Gbetagamma. *Sci Signal* **9**, ra22 (2016).

57. Nobles, M., Montaigne, D., Sebastian, S., Birnbaumer, L. & Tinker, A. Differential effects of inhibitory G protein isoforms on G protein-gated inwardly rectifying K^+ currents in adult murine atria. *American Journal of Physiology-Cell Physiology* **314**, C616-C626 (2018).

58. Mumby, S.M. & Gilman, A.G. Synthetic peptide antisera with determined specificity for G protein alpha or beta subunits. *Methods Enzymol* **195**, 215-33 (1991).

59. McAlister, G.C. et al. MultiNotch MS3 Enables Accurate, Sensitive, and Multiplexed Detection of Differential Expression across Cancer Cell Line Proteomes. *Analytical Chemistry* **86**, 7150-7158 (2014).

60. Mumby, S.M. & Linder, M.E. Myristoylation of G-protein alpha subunits. *Methods Enzymol* **237**, 254-68 (1994).

61. Dessauer, C.W. Kinetic analysis of the action of P-site analogs. *Methods Enzymol* **345**, 112-26 (2002).

62. Jo, S., Kim, T., Iyer, V.G. & Im, W. CHARMM-GUI: a web-based graphical user interface for CHARMM. *J Comput Chem* **29**, 1859-65 (2008).

63. Hess, B., Kutzner, C., van der Spoel, D. & Lindahl, E. GROMACS 4: Algorithms for Highly Efficient, Load-Balanced, and Scalable Molecular Simulation. *J Chem Theory Comput* **4**, 435-47 (2008).

64. Huang, J. et al. CHARMM36m: an improved force field for folded and intrinsically disordered proteins. *Nat Methods* **14**, 71-73 (2017).

65. Berendsen, H.J.C.P., J.P.M.; van Gunsteren, W.F.; DiNola, A.; Haak, J.R. Molecular dynamics with coupling to an external bath. *The Journal of Chemical Physics* **81**, 3684-3690 (1984).

66. Andersen, H.C. Rattle: A “velocity” version of the shake algorithm for molecular dynamics calculations. *Journal of Computational Physics* **52**, 24-34 (1983).

67. T. Darden, D.Y., L. Pedersen. Particle mesh Ewald: An N ·log(N) method for Ewald sums in large systems. *Journal of Chemical Physics* **98**, 10089–10092 (1993).

68. Evans, D.J.H., B.L. The Nose–Hoover thermostat. *The Journal of Chemical Physics* **83**, 4069-4074 (1985).

69. Parrinello, M.R., A. Polymorphic transitions in single crystals: A new molecular dynamics method. *Journal of Applied Physics* **52**, 7182-7190 (1981).

70. Petrova, S.S.S.e., A.D. The Origin of the Method of Steepest Descent. *Historia Mathematica* **24**, 361-375 (1997).

71. Gogoshin, G.B., E.; Rodin, A.S. New Algorithm and Software (BNOmics) for Inferring and Visualizing Bayesian Networks from Heterogeneous Big Biological and Genetic Data. *Journal of Computational Biology* **24**, 340-356 (2017).

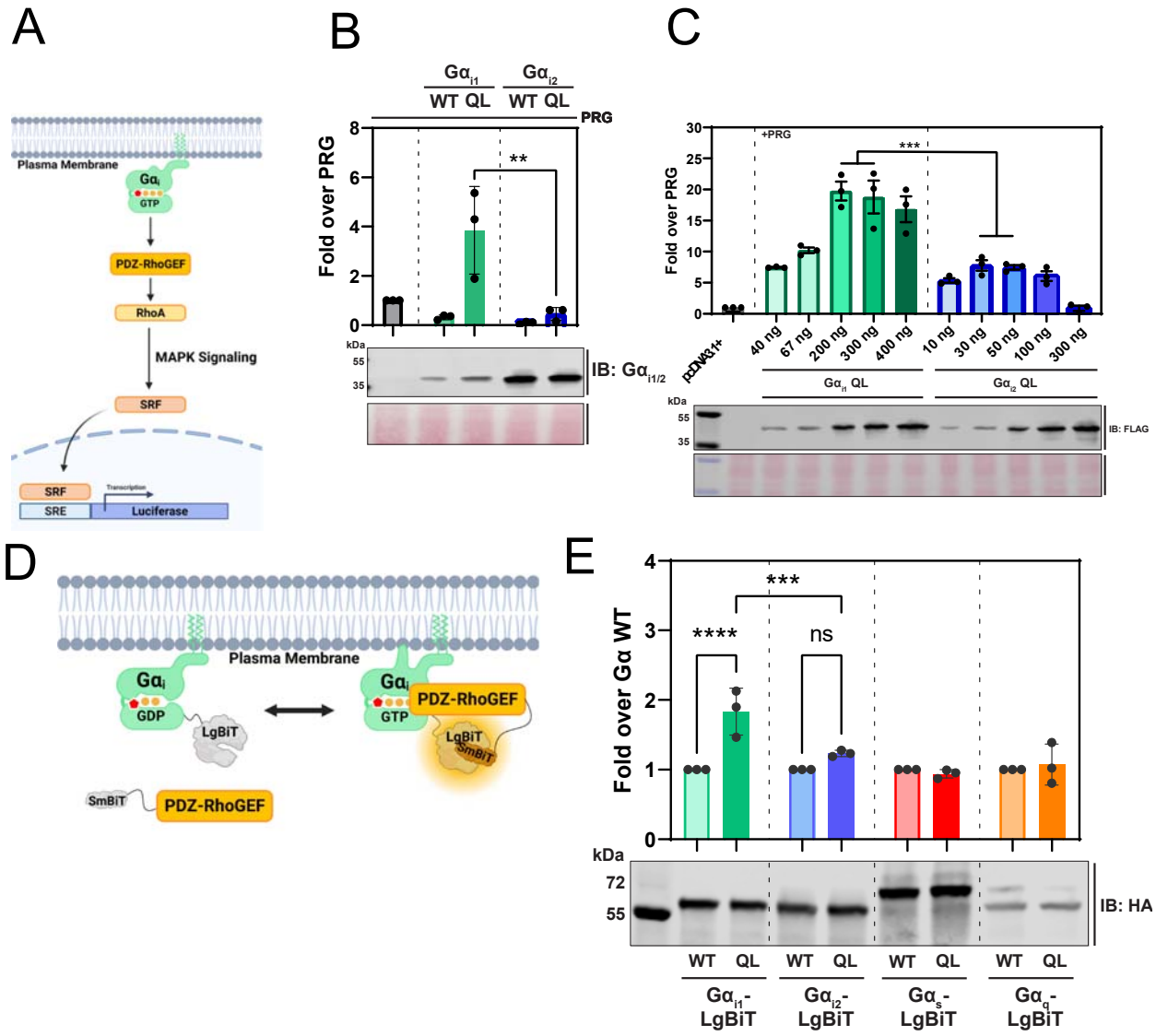

Figure 1. Gα$_{i1}$ more efficiently interacts with PRG than Gα$_{i2}$.

A) Diagram of the SRE luciferase used to assess Gα regulation of PRG. HEK293 cells were co-transfected with control plasmid pcDNA 3.1 or Gα plasmids as indicated, PRG, and an SRE luciferase reporter plasmid. 24 h after transfection One-Glo luciferase reagent was added and luminescence was measured using a plate reader.

B) Comparison of Gα$_{i1}$ and Gα$_{i2}$ which were transfected as indicated. All wells were transfected with PRG. Fold over PRG was calculated as the luminescent signal with Gα subunits co-transfected with PRG divided by the signal with PRG co transfected with control pcDNA 3.1 plasmid.

C) Cells were transfected with the indicated amount of FLAG-Gα$_{i1}$ QL or FLAG-Gα$_{i2}$ QL adjusted to achieve equivalent expression as shown in the flag western blot shown in the bottom panel. To calculate the significance in the difference in maximal stimulation the values for 200 and 300 ng of Gα$_{i1}$ plasmid were averaged and compared to the average of the 30 and 50 ng values for Gα$_{i2}$. T-test *** P<0.001.

1026 **D)** Diagram of the $G\alpha_i$-LgBiT complementation assay used with $G\alpha_i$ fused to LgBiT and
1027 PRG with N-terminal fusion of SmBiT peptide natural peptide sequence (PRG-SmBiT).
1028 **E)** The indicated plasmids were co-transfected into HEK293 cells with PRG-SmBiT. 24
1029 h after transfection cells were transferred into a 96 well plate and furimazine substrate
1030 was added for 15 min prior to measurement of luminescence in a plate reader.
1031 All experiments were performed with at least three biological replicates of assays
1032 performed in triplicate. Unless otherwise indicated data was analyzed with a one-way
1033 ANOVA with a Šídák post-test. ** $P<0.01$ and ****$P<.0001$.
1034

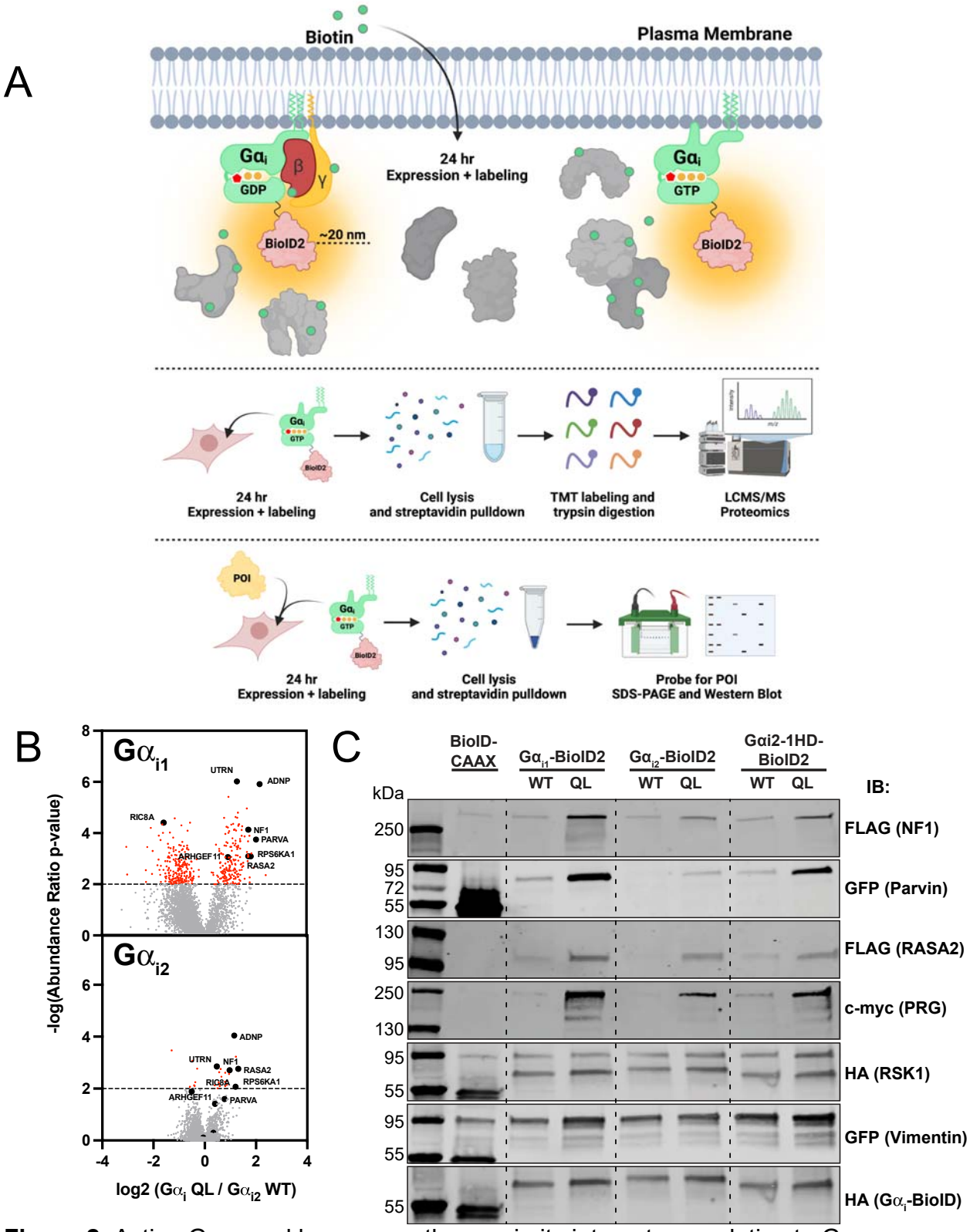

Figure 2. Active $G\alpha_{i2}$ weakly engages the proximity interactome relative to $G\alpha_{i2}$.
A) Experimental outline for biotin proximity labeling assays.

1038 **B)** The indicated HA-Gα_i-BioID2 constructs were transiently transfected into HT1080
1039 cells, in triplicate for each condition for 24 h followed by isolation of biotinylated proteins
1040 and analysis by TMT Mass Spectrometry. To control for differences in overall
1041 biotinylation each sample was normalized based on the total spectral counts for all of
1042 the proteins identified (~4000 proteins). Spectral counts were then analyzed as the ratio
1043 of samples transfected with the Gα_i-QL plasmids relative to samples transfected with
1044 Gα_{i2} WT. The dashed line indicates a p value of 0.01 and all statistically significant
1045 proteins are colored in red.
1046 **C)** The indicated Gα_i-BioID2 constructs were co-transfected with the indicated epitope-
1047 tagged protein into HEK293 cells. 24 h after transfection biotinylated proteins were
1048 isolated with streptavidin beads and the followed by western blotting to determine the
1049 amount of biotinylated target protein pulled down. Shown is a representative western
1050 blot of an experiment performed twice.
1051

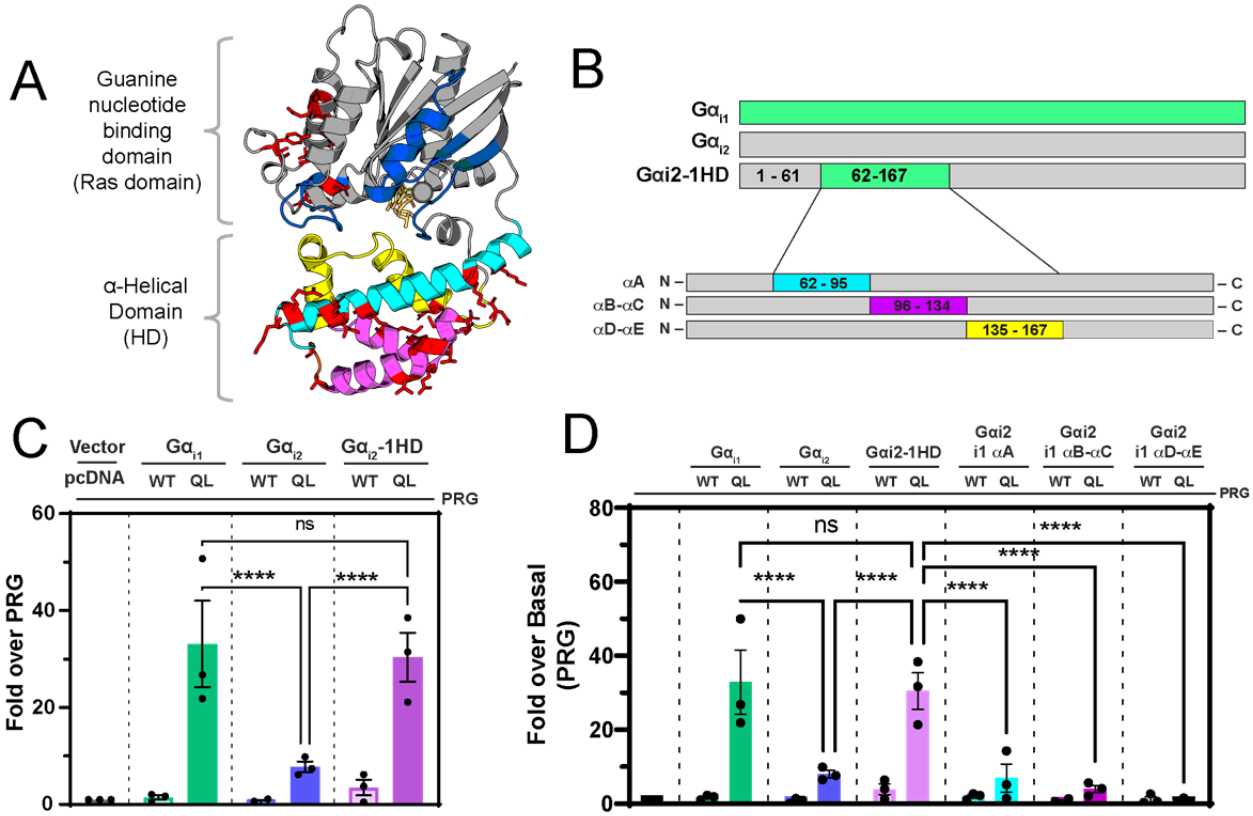

Figure 3. Substitution of the $G\alpha_{i1}$ helical domain into $G\alpha_{i2}$ partially restores activation of PRG.

A) Diagrammatic representation of the $G\alpha_{i1}$ structure. In cyan, magenta, and yellow are subdivisions of the helical domain. Switch I-III are in blue. Red stick amino acids are amino acids conserved between $G\alpha_{i1}$ and $G\alpha_{i3}$ but not $G\alpha_{i2}$. PDB: 1CIP.
B) Diagram of the constructs used in these experiments.
C) and D) The indicated constructs were co-transfected with PRG and SRE-Luc and the assay was performed as in Fig. 1. Western blots for expression and cAMP assays are in Fig. S1 A,B,C and D. E)
All SRE-luc experiments were performed with 3 biological replicates performed in triplicate. Data are +/-SEM analyzed by One-way ANOVA with Šídák post-test. **** P<0.0001.

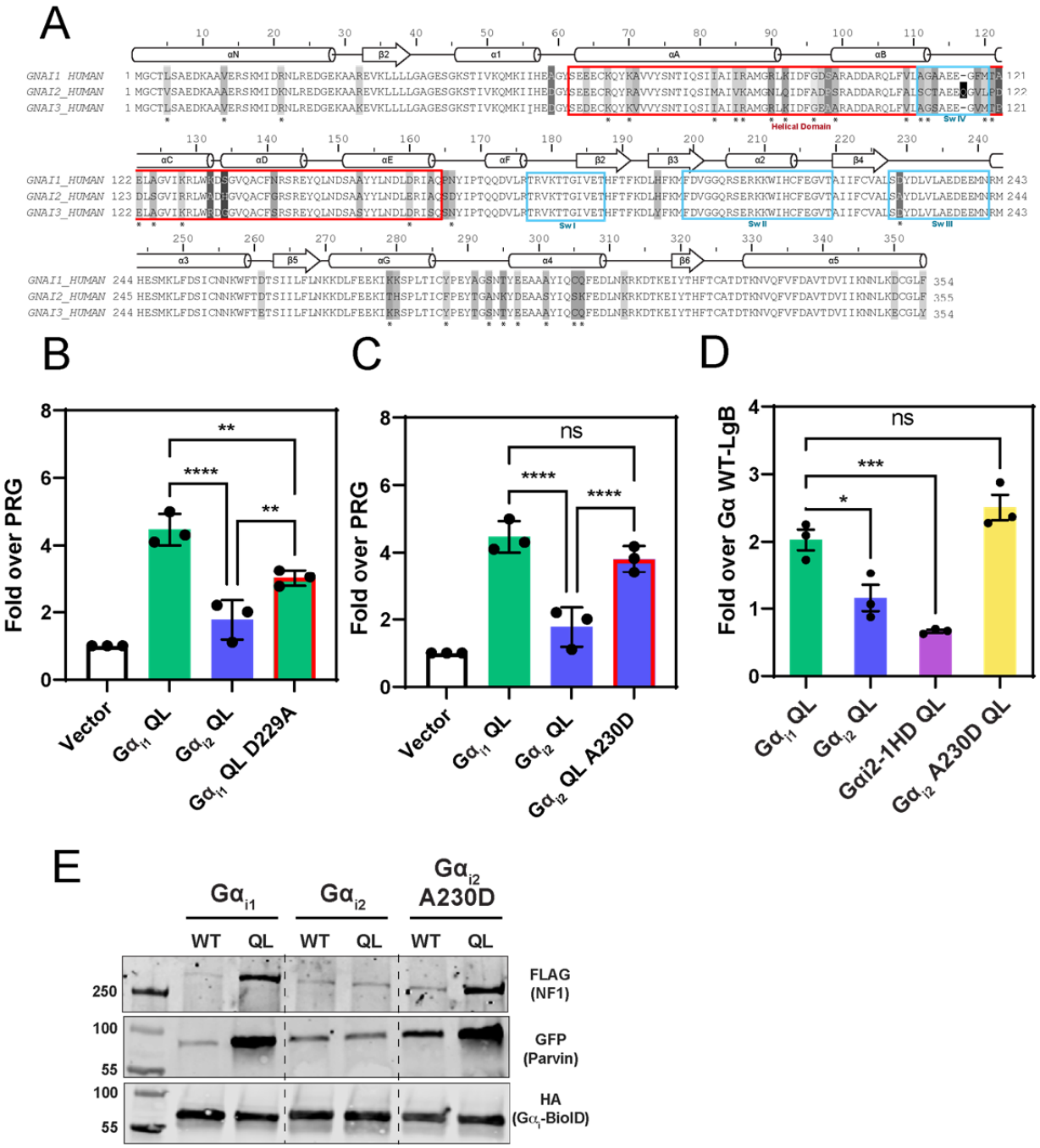

Figure 4. Gα$_{i1}$ D229/Gα$_{i2}$ A230$^{s4h3.3}$ in the Ras-like domain is critical for differences in PRG activation.

A) Alignment of human Gα$_{i1}$, Gα$_{i2}$, and Gα$_{i3}$. Boxed in blue are the Gα$_i$ switch regions. The helical domain is boxed in red. Starred (*) amino acids are identical in Gα$_{i1}$ and Gα$_{i3}$ but different in Gα$_{i2}$.

B) Mutation of Gα$_{i1}$ D229$^{s4h3.3}$ to the corresponding A in Gα$_{i2}$ (A230$^{s4h3.3}$) reduces the ability to activate PRG.

C) Mutation of $G\alpha_{i2}$ A230 to the corresponding D in $G\alpha_{i1}$ (D229) enhances the ability of $G\alpha_{i2}$ to activate PRG.
D) Mutation of $G\alpha_{i2}$ A230 to the corresponding D in $G\alpha_{i1}$ (D229) enhances interactions between $G\alpha_{i2}$-LgBiT and PRG-SmBiT in the luciferase complementation assay.
E) Mutation of $G\alpha_{i2}$ A230 to the corresponding D in $G\alpha_{i1}$ (D229) enhances interactions with other proteins in the $G\alpha_i$ proximity interactome. Shown is representative western blot for an experiment performed twice. All SRE-luc and complementation experiments were performed with 3 biological replicates performed in triplicate. Data are +/- SEM analyzed by One-way ANOVA with Šídák post-test; * $P<0.05$, ** $P<0.01$, *** $P<0.001$,**** $P<0.0001$.

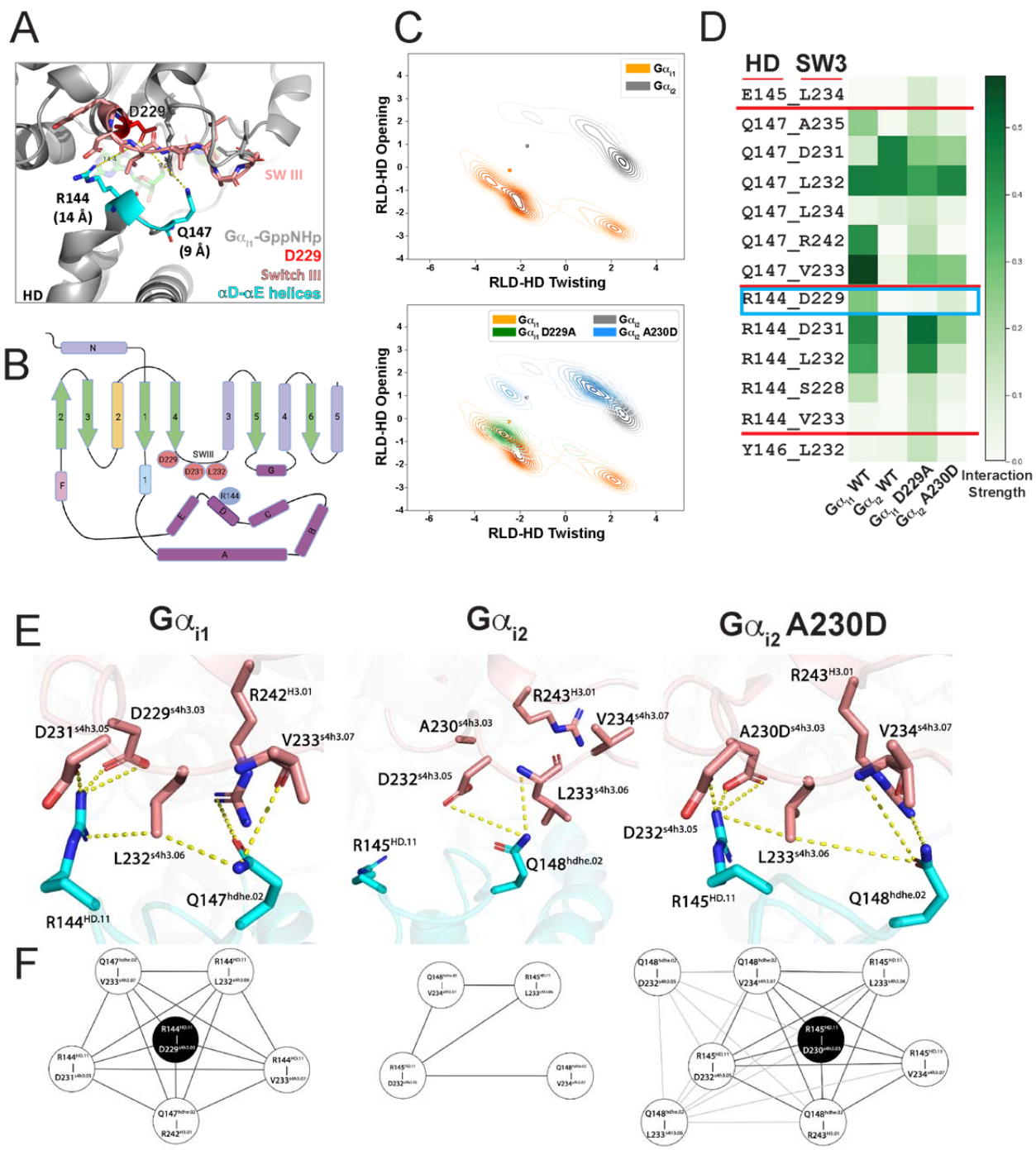

Figure 5. Molecular dynamics simulations and Bayesian network analysis reveal an interaction network that is not apparent in three dimensional crystal structures in the GTP bound state.

A) Diagram of a structure of $G\alpha_{i1}$-GTP showing the distance between D229 and the nearest HD residues.

B) Ribbon representation of Gα subunit structure highlighting key amino acids at the Switch III-helical domain interface.

C) Principal component analysis of $G\alpha_{i1}$-GTP vs. $G\alpha_{i2}$-GTP.

D) Interaction frequency heat map of amino acid interactions between Switch III amino acids and amino acids in the HD comparing the GTP bound states of $G\alpha_{i1}$, $G\alpha_{i2}$, $G\alpha_{i1}$ D229A, and $G\alpha_{i2}$ A230D.
E) Diagram of interdomain interactions involving D229 in $G\alpha_{i1}$-GTP (top panel) and A230 in $G\alpha_{i2}$-GTP (middle panel) and $G\alpha_{i2}$-GTP A230D (right panel).
F) Bayesian networks showing interdomain interactions driven by D229 and HD R144 in $G\alpha_{i1}$-GTP(left panel), In $G\alpha_{i2}$ A230 cannot interact with R145 weakening the overall interaction network (middle panel), Substitution of D for A230 in $G\alpha_{i2}$-GTP leads to interactions with R145 stabilizing the interaction network between the HD and Switch III. Each node represents a contact made between the HD and Switch III, the thickness of the edge connecting the nodes indicates whether the edge was present in the $G\alpha_{i1}$ network.

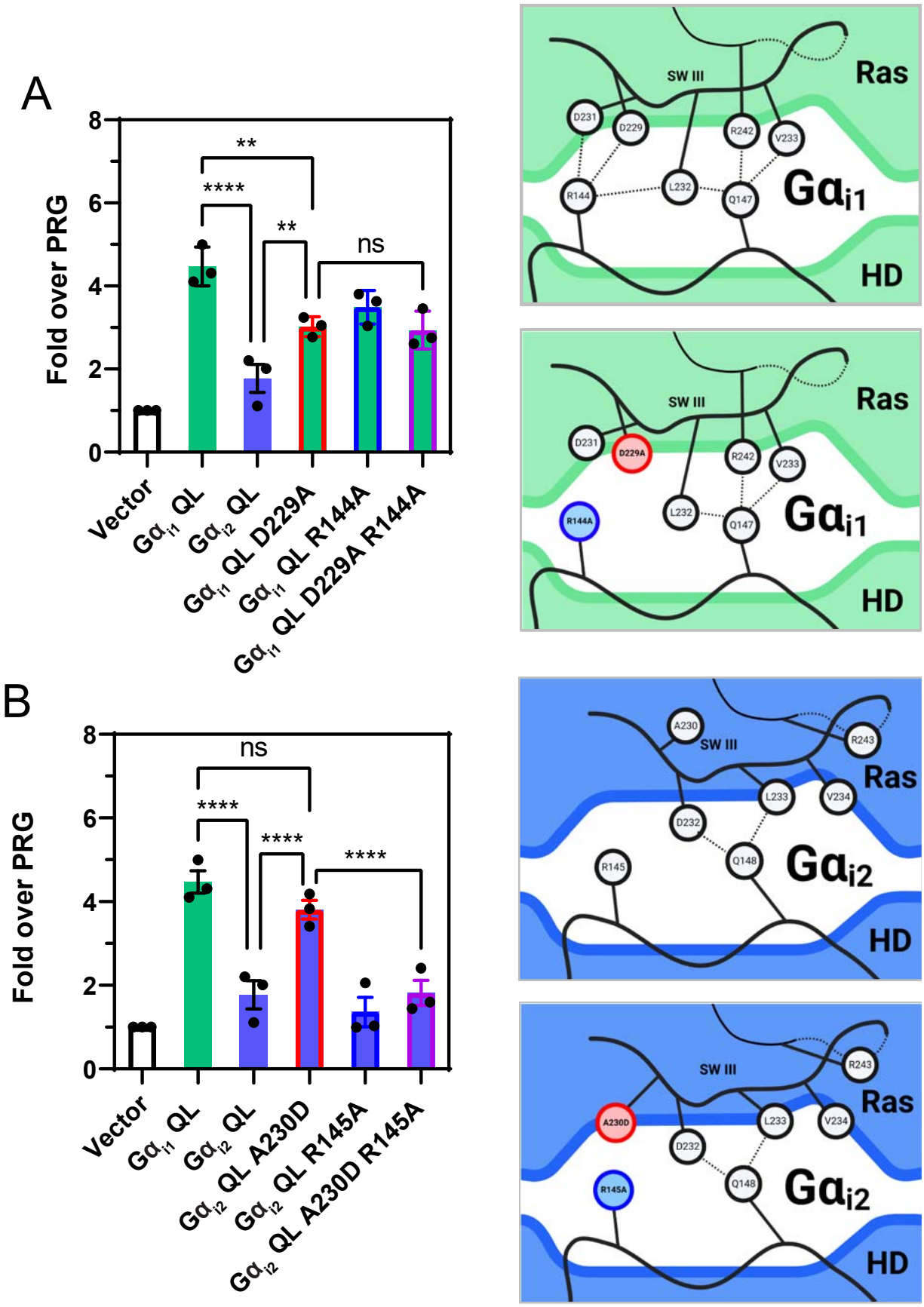
A
Fold over PRG
8
6
4
2
0
**
****
**
ns
Vector
Gαi1 QL
Gαi2 QL
Gαi1 QL D229A
Gαi1 QL R144A
Gαi1 QL D229A R144A
SW III
Ras
D231
D229
R242
V233
R144
L232
Q147
Gαi1
HD
D229A
R144A
B
ns
****
****
****
Vector
Gαi1 QL
Gαi2 QL
Gαi2 QL A230D
Gαi2 QL R145A
Gαi2 QL A230D R145A
A230
R243
L233
V234
D232
R145
Q148
Gαi2
A230D
R145A

1145

1146 **Figure 6.** Gα$_{i1}$ D229/Gα$_{i2}$ A230 controls HD-RLD interdomain interactions.

1147 **A)** SRE luciferase assay showing PRG activation by QL versions of Gα$_{i1}$, Gα$_{i2}$, Gα$_{i1}$
1148 D229A, Gα$_{i1}$ R144A, and Gα$_{i1}$ D229A-R144A (left panel). The top right panel is a
1149 diagram of the WT Gα$_{i1}$ interaction network. The bottom right panel is a diagram of the
1150 Gα$_{i1}$ interaction network indicating the amino acid substitutions in red and blue.
1151 **B)** SRE luciferase assay showing PRG activation by QL versions of Gα$_{i1}$, Gα$_{i2}$, Gα$_{i2}$
1152 A230D, Gα$_{i2}$ R145A, and Gα$_{i2}$ A230D-R145A. The top right panel is a diagram of the
1153 WT Gα$_{i2}$ interaction network. The bottom right panel is a diagram of the Gα$_{i2}$ interaction
1154 network indicating the amino acid substitutions in red and blue. Experiments were
1155 performed with 3 biological replicates performed in triplicate. Data are +/- SEM
1156 analyzed by One-way ANOVA with Šídák post-test; * P<0.05, ** P<0.01, ***
1157 P<0.001,**** P<0.0001.
1158

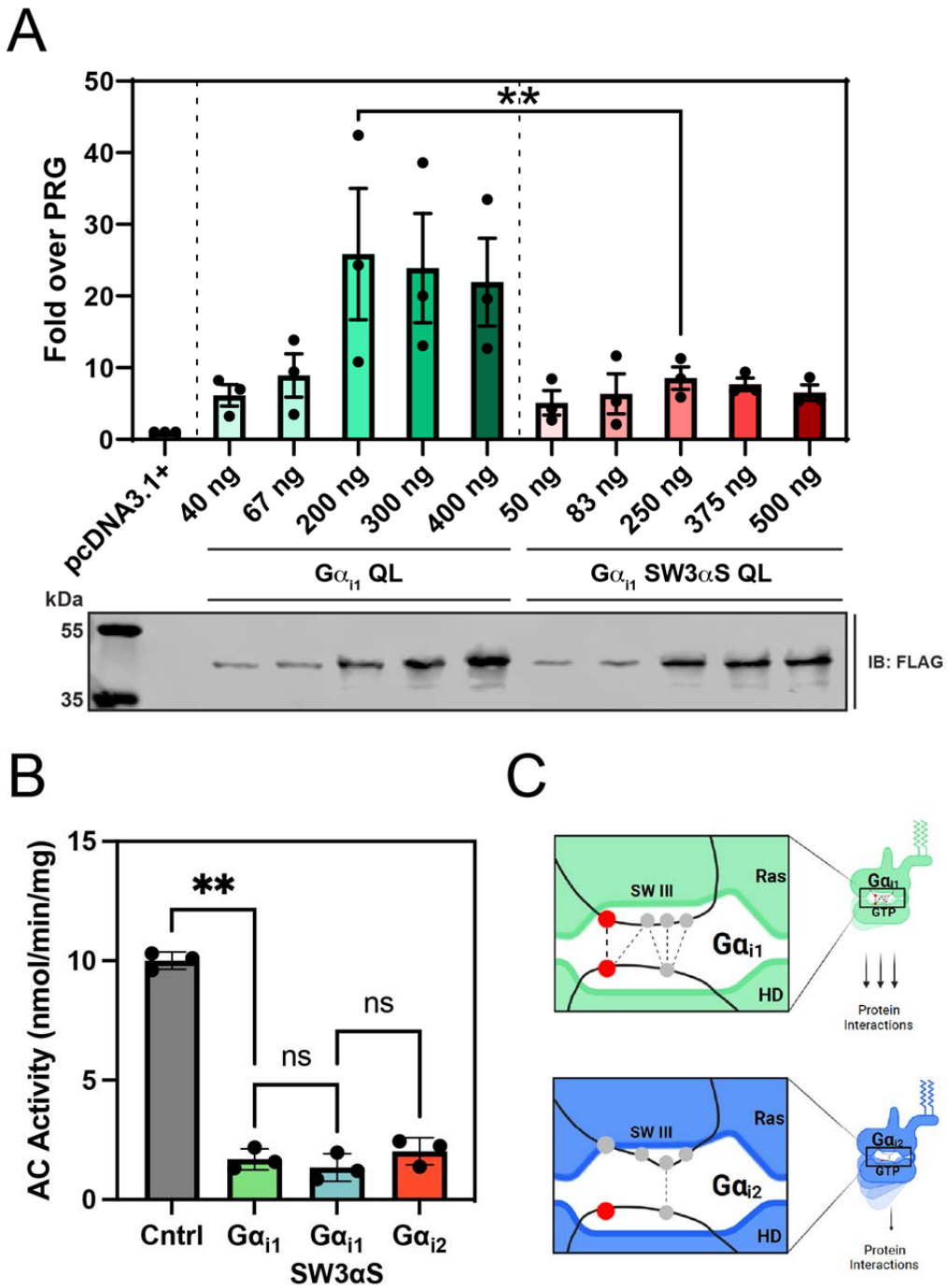

Figure 7. Gα$_{i1}$ Switch III is critical for activation of PRG.

A) Switch III amino acids in Gα$_{i1}$ were substituted with the cognate amino acids in Gα$_s$ and assayed for PRG activation using the SRE-luc assay. Experiments were performed with 3 biological replicates performed in duplicate. Data are +/- SEM analyzed by One-way ANOVA with Šídák post-test; * P<0.05, ** P<0.01, *** P<0.001,**** P<0.0001.

B) Structural representation of active Gα$_{i1}$ and active Gα$_{i1}$ with Gα$_s$ substitutions made in Gα$_{i1}$ Switch III. Gα$_{i1}$ is grey, the αD helix in the HD is shown in tan for orientation, Gα$_{i1}$

1167 Switch III residues are shown in green sticks, and the $G\alpha_{i1}$ residues mutated to
1168 corresponding residues in $G\alpha_s$ are in pink. PDB ID: 1CIP. **C)** Sf9 membranes
1169 expressing hAC6 were assayed in the presence of 10 mM $MgCl_2$, 250 μM ATP and 30
1170 nM $G\alpha_s$·GTPγS in the absence and presence of 1μM myr$G\alpha_{i1}$, myr$G\alpha_{i1}$SW3αS, or
1171 myr$G\alpha_{i2}$. mean ± SD, n=3 performed in duplicate. **D)** Overall model of the interactions
1172 between the AHD and RLD domains of $G\alpha_i$ subunits that modulate differential
1173 interactions between Gai subtypes and downstream proteins.
1174

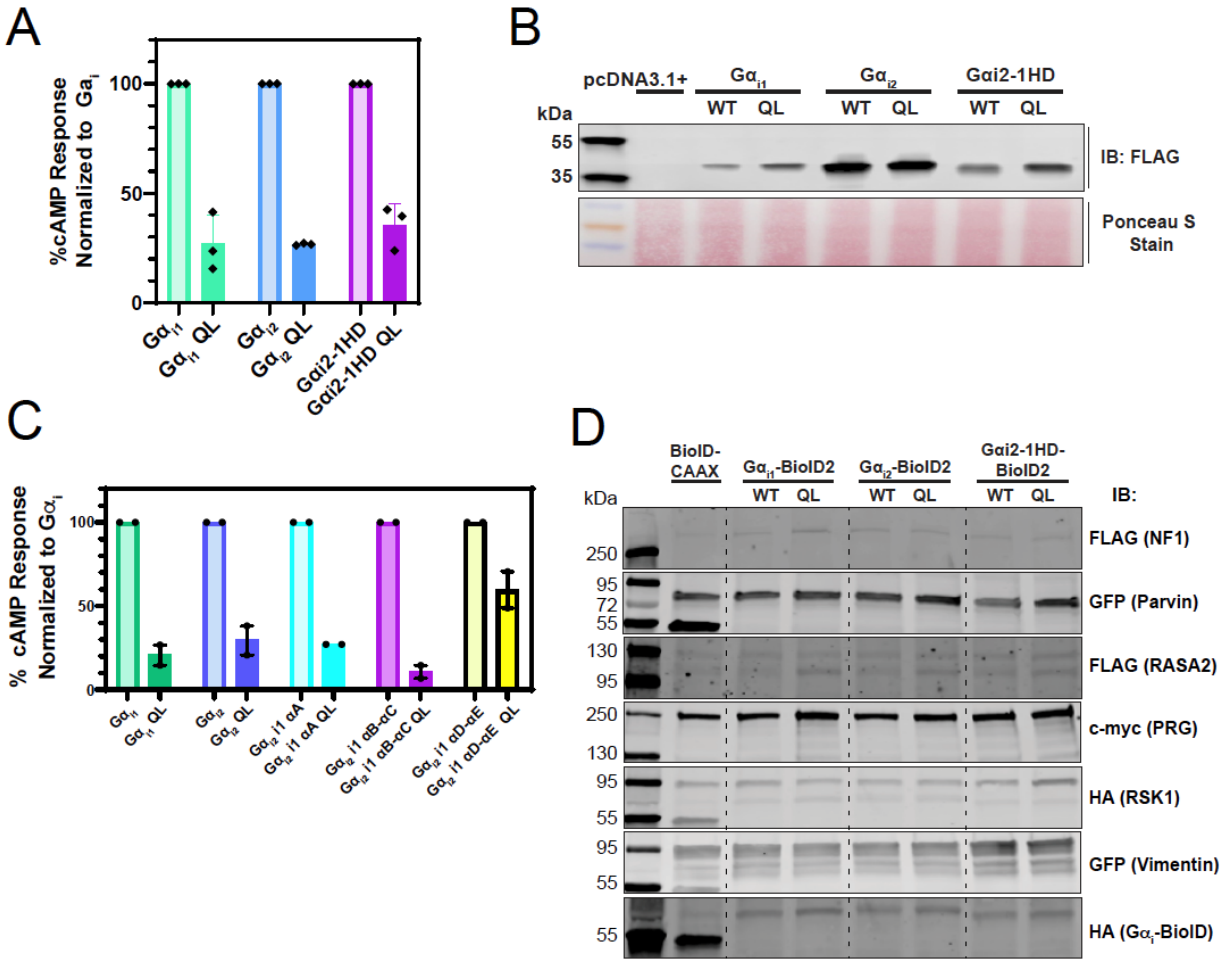

Figure S1.Supporting data for Figure 3. A) cAMP assay measuring the activities of proteins tested in Fig. 3C. B) Western blot showing expression of proteins used in Fig. 3C. C) cAMP assay measuring activities of chimeric proteins used in Fig. 3D. D) Input western blots for BioID2 experiments in Fig. 3E.

1193

1194

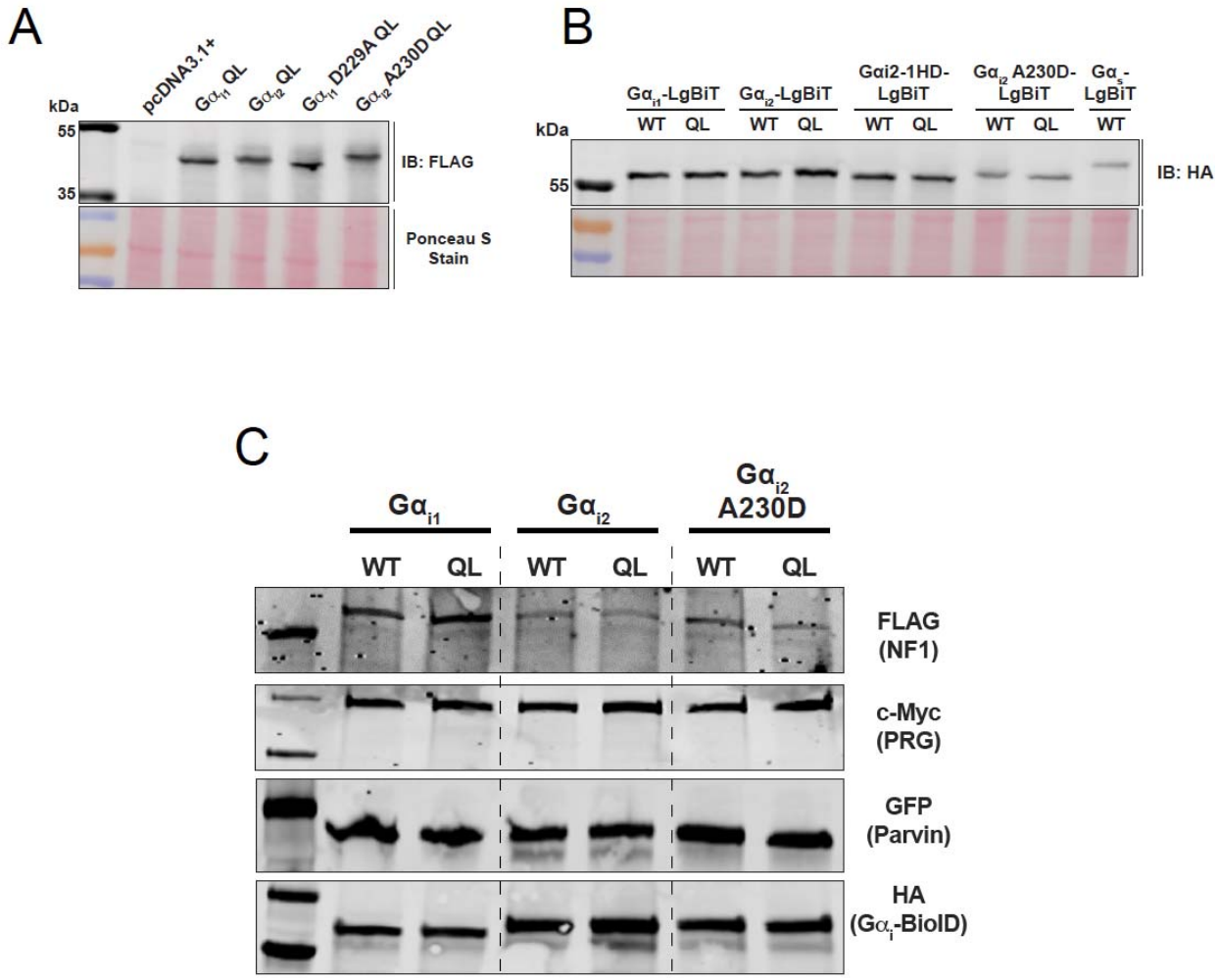

1195

1196

1197 **Figure S2**. Supporting data for figure 4. A) Western blot for proteins used in Fig. 4B and
1198 C. B) Western blot for proteins used in Fig. 4D. C) Input western blots for BioID2
1199 experiments in Fig. 4E.

1200

1201

1202

1203

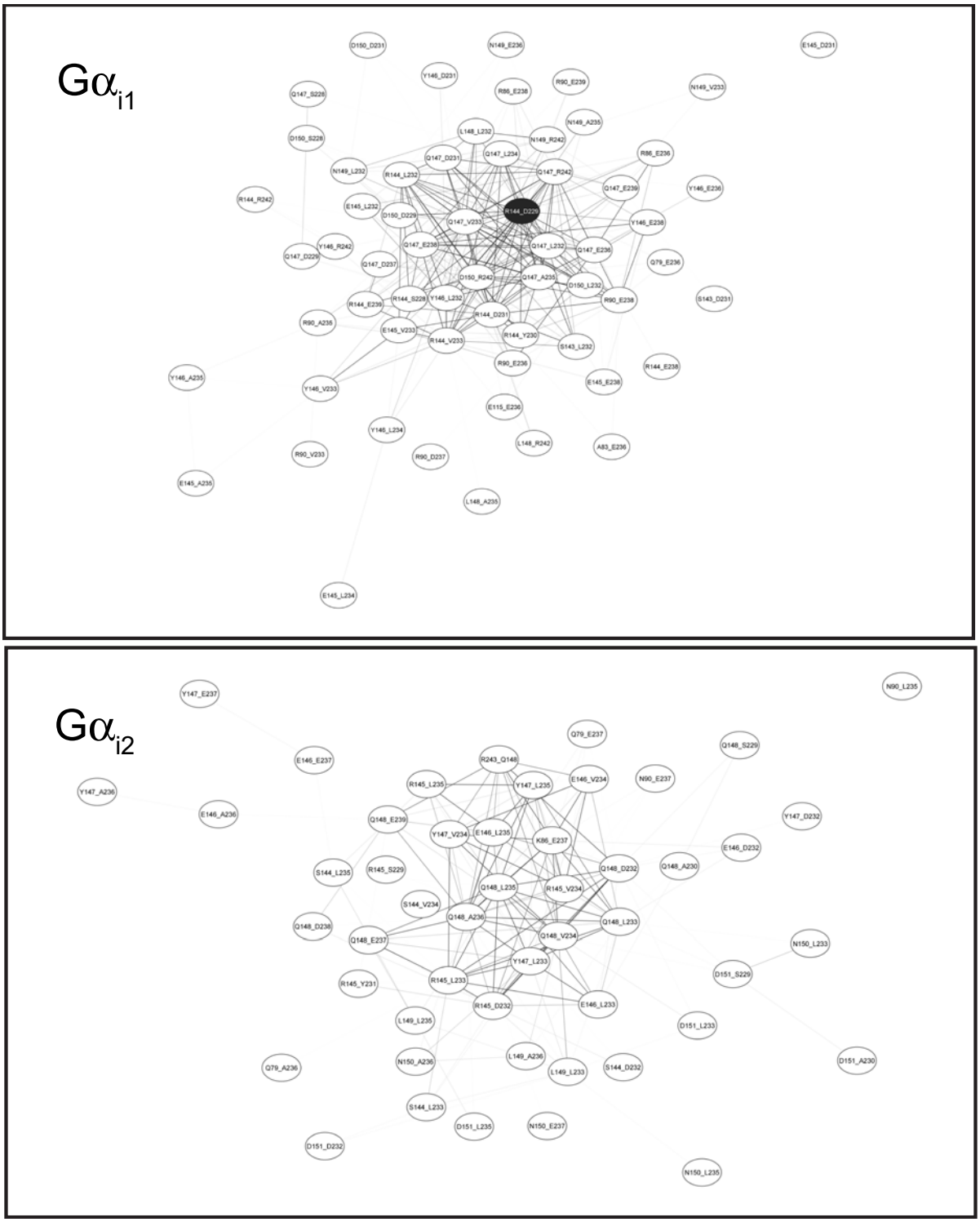

Figure S3. Full Bayesian networks for $G\alpha_{i1}$ and $G\alpha_{i2}$ supporting figure 5.

1208

1209

1210

1211

1212

1213

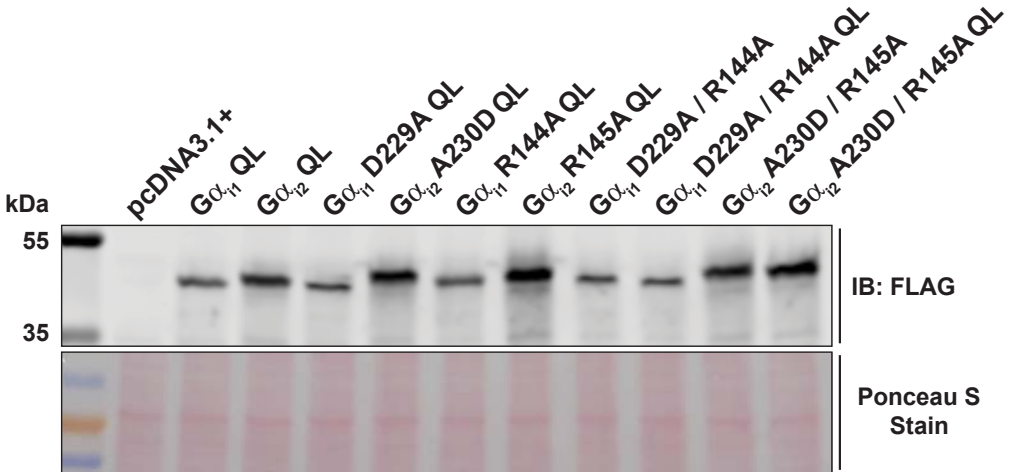

1214

1215 **Figure S4.** Supporting data for Figure 6. A) Western blot for protein expression for Fig.
1216 6A and B.

1217

1218

1219

1220

1221

1222

1223

1224

1225

1226

1227

1228

	HD.11		s4h3.3
GNAS2	N		S
GNAL	N		S
GNAI1	R	—	D
GNAI2	R		A
GNAI3	R	—	D
GNAT1	S		A
GNAT2	A		A
GNAT3	S		A
GNAO	R		G
GNAZ	S		G
GNAQ	R	—	E
GNA11	R	—	E
GNA14	R	—	E
GNA15	R	—	E
GNA12	S		E
GNA13	R	—	E

Residue coloring scheme

Aliphatic/hydrophobic	ILVAM
Aromatic	FWY
Positive	KRH
Negative	DE
Hydrophilic	STNQ
Conformationally Special	PG
Cysteine	C

Figure S5. Alignments of all the G protein α subunit families highlighting the presence or absence of ionic lock amino acids HD.11 in the helical domain and s4h3.3 in the RLD.